Atmos. Chem. Phys., 13, 11905–11923, 2013
www.atmos-chem-phys.net/13/11905/2013/
doi:10.5194/acp-13-11905-2013

Atmospheric Chemistry and Physics Open Access

The metastable $HCl \cdot 6H_2O$ phase – IR spectroscopy, phase transitions and kinetic/thermodynamic properties in the range 170–205 K

S. Chiesa[1,2] **and M. J. Rossi**[1,*]

[1]Laboratoire de Pollution Atmosphérique et du Sol (LPAS), Station 6, LPAS/ISTE/ENAC, Swiss Federal Institute of Technology (EPFL), Lausanne, Switzerland
[2]Groupe de Recherche en Bioénergie et Planification énergétique, ENAC, Swiss Federal Institute of Technology (EPFL), 1004 Lausanne, Switzerland
[*]now at: Laboratorium für Atmosphärenchemie (LAC), OFLA008, Paul Scherrer Institut (PSI), 5232 Villigen PSI, Switzerland

Correspondence to: M. J. Rossi (michel.rossi@psi.ch)

Received: 2 May 2013 – Published in Atmos. Chem. Phys. Discuss.: 4 July 2013
Revised: 5 November 2013 – Accepted: 6 November 2013 – Published: 9 December 2013

Abstract. In this laboratory study a multidiagnostic experimental approach including Fourier transform infrared (FTIR) absorption of 1 to 2 µm thick polycrystalline ice films, residual gas mass spectrometry (MS) and total pressure measurement were employed. Both amorphous HCl–H_2O and crystalline HCl hexahydrate ($HCl \cdot 6H_2O$) have been investigated. After controlled doping with HCl and evaporation of excess H_2O from the ice film, transmission FTIR of pure $HCl \cdot 6H_2O$ films and use of calibrated mass spectrometry enabled the measurement of differential (peak) IR cross sections at several mid-IR frequencies, for example $\sigma = (6.5 \pm 1.9) \times 10^{-19}$ cm^2 molec^{-1} at 1635 cm^{-1}. Two types of kinetic experiments on pure $HCl \cdot 6H_2O$ have been performed under SFR conditions: (a) evaporation of pure $HCl \cdot 6H_2O$ over a narrow T range after evaporation of excess H_2O, and (b) observation of the phase transition from crystalline $HCl \cdot 6H_2O$ to amorphous HCl–H_2O under H_2O-rich conditions at increasing T. The temperature dependence of the zero-order evaporation flux of HCl in pure $HCl \cdot 6H_2O$ led to $\log J_{ev}$ molec cm^{-2} s^{-1} $= (36.34 \pm 3.20) - (80\,810 \pm 5800)/2.303\,RT$ with $R = 8.314$ JK^{-1} mol^{-1}, which turned out to be rate-limiting for evaporation. $HCl \cdot 6H_2O$ has a significant intrinsic kinetic barrier to HCl evaporation of 15.1 kJ mol^{-1} in excess of the HCl sublimation enthalpy of 65.8 kJ mol^{-1} at 200 K but is kinetically unstable (metastable) at $T \geq 173$ K. The atmospheric importance of $HCl \cdot 6H_2O$ is questioned in view of its large nucleation barrier and its dependence on T and P(HCl) compared to the amorphous HCl–H_2O phase at upper tropospheric–lower stratospheric (UT/LS) conditions.

1 Introduction

Heterogeneous chemistry on ice surfaces has been intensely studied since the discovery of its role in the processes occurring on polar stratospheric clouds (PSCs). These ultimately lead to the transformation of reservoir species of chlorine, such as HCl and $ClONO_2$, into atomic chlorine in the presence of actinic radiation, which is known to destroy the atmospheric ozone layer through a catalytic cycle (Solomon, 1990). PSCs form during the cold polar winter and are classified according to their composition (Zondlo et al., 2000). They consist either of crystalline HNO_3/H_2O (type Ia), of ternary $H_2SO_4/HNO_3/H_2O$ supercooled solutions (type Ib), or of pure H_2O ice particles (type II). Potential heterogeneous reactions involving adsorbed HCl (HCl(s)) and leading to chlorine activation occurring on PSCs include

$$ClONO_2\,(g) + HCl\,(s) \rightarrow Cl_2\,(g) + HNO_3\,(s), \qquad (R1)$$

$$HOCl\,(g) + HCl\,(s) \rightarrow Cl_2\,(g) + H_2O\,(s), \qquad (R2)$$

$$N_2O_5\,(g) + HCl\,(s) \rightarrow ClNO_2\,(g) + HNO_3\,(s). \quad \text{(R3)}$$

These heterogeneous reactions are faster by orders of magnitude than their corresponding gas-phase reactions (L. T. Molina et al., 1985; M. J. Molina et al., 1987; Friedl et al., 1986) and are relevant for the upper tropospheric–lower stratospheric (UT/LS) region of the planetary atmosphere (Hanson and Ravishankara, 1992; Lee et al., 1999; Hynes et al., 2001; Haq et al., 2002; Huthwelker et al., 2004). The properties of the condensed phase are of great importance since different molecular structures sharing the same stoichiometric composition may have different chemical properties, a point of view ignored in earlier studies. Apart from the stratosphere, the HCl–ice system may also be relevant for the upper troposphere (UT) (Borrmann et al., 1996; Solomon et al., 1997).

Investigations have been carried out over the past years by employing particle surrogates or model stratospheric films grown in the laboratory. The advantage of such an approach is that controlled experimental conditions allow for the study of thermodynamic and kinetic properties of the condensate. Studies have been conducted employing flow tubes at low pressure (Abbatt et al., 1992) or high-vacuum chambers in which pure ice films of different thicknesses have been grown and subsequently exposed to HCl vapor. Among the latter, the majority have used Fourier transform infrared (FTIR) spectroscopy as a tool to qualitatively identify the molecular structure of HCl–H_2O in situ. In these studies, transmission spectroscopy (Ritzhaupt and Devlin, 1991; Delzeit et al., 1993; Koehler et al., 1993; Xueref and Dominé, 2003) as well as reflection–absorption spectroscopy (Graham and Roberts, 1995, 1997; Banham et al., 1996) have been performed and characteristic IR spectral features of amorphous and crystalline acid hydrates have been found. When adsorbed on ice, HCl can give rise to a number of amorphous mixtures of different $HCl : H_2O$ ratio, depending on the amount of adsorbed HCl, and to two crystalline hydrates, namely the crystalline hexahydrate ($HCl \cdot 6H_2O$) and trihydrate ($HCl \cdot 3H_2O$). A HCl–H_2O phase diagram has been constructed (Molina, 1994) that shows that HCl trihydrate exists at higher HCl concentrations than the hexahydrate phase and does therefore not seem relevant for the atmosphere. The above-cited spectroscopic studies usually employed amorphous ice at low temperature rich in dangling OH bonds (Buch and Devlin, 1991) as the substrate exposed to HCl vapor, while we use polycrystalline hexagonal ice I_h in the present study. The importance of the ice substrate structure prior to doping with HCl has been pointed out by Sadtchenko et al. (2000) and McNeill et al. (2007) because it may influence the nature of the phase that may form.

X-ray absorption spectroscopy has provided the method of choice to distinguish the molecular from the ionic nature of the HCl–H_2O system. Near-edge X-ray fine structure spectroscopy (NEXAFS) is sensitive to both surface and bulk regions of the sample and has shown that at $T > 90$ K, HCl adsorbed on the ice surface and present in the bulk form solvated ionic complexes of the type $H_3O^+Cl^- \cdot nH_2O$ and is thus completely dissociated (Parent and Laffon, 2005; Bournel et al., 2002). HCl hydrogen bonding with dangling OH bonds of H_2O at 90 K has been found to be responsible for only 20 % (upper limit) of the ionization events, while another mechanism must drive the remaining ionic dissociation into Cl^- and H_3O^+ within the bulk, presumably ionic solvation. Therefore, dangling OH bonds are probably not involved in the driving force for the strong HCl–ice interaction at the HCl–H_2O condensed interface in contrast to expectation based on molecular modeling of the HCl–ice surface.

Recently, the uptake of acidic gases including HCl on ice has been exhaustively summarized in view of abundant experimental facts (Huthwelker et al., 2006). As an example, the HCl uptake on the crystalline and amorphous phases of the HCl–H_2O system has been evaluated using laser-induced thermal desorption (Foster et al., 1997) as a tool to monitor the composition of the HCl–H_2O films under study. Temperature-programmed desorption measurements (Banham et al., 1996; Graham and Roberts, 1995, 1997; Sadtchenko et al., 2000) have shown that two different desorption patterns are found, depending on the amount of doping of the ice film with HCl in the case of a limited exposure to HCl, and a single peak is found around 187 K, while in the case of a prolonged exposure, two different desorption peaks are visible at 160 and 190 K, where the first refers to a conversion of a lower hydrate structure into a new amorphous $6 : 1$ $H_2O : HCl$ phase.

Combined experimental reflection–absorption IR spectroscopy (RAIRS) and theoretical DFT studies by Ortega et al. (2004, 2005) have helped to understand the molecular and lattice vibrations that contribute to the IR absorption spectra of the HCl trihydrate and hexahydrate crystals. Other experiments have addressed the behavior of HNO_3-doped ice when exposed to HCl vapors (Ortega et al., 2006; Hynes et al., 2002).

It is crucial to determine which phase in the HCl–H_2O system is relevant under atmospheric conditions because, taking the example of Reaction (R1), the structure controls its heterogeneous reactivity (McNeill et al., 2006). It turns out that the amorphous HCl–H_2O phase is more reactive than crystalline $HCl \cdot 6H_2O$ under comparable HCl and H_2O vapor pressures. As previously noted (Koehler et al., 1993; McNeill et al., 2007), $HCl \cdot 6H_2O$ nucleation may require very low temperatures and may therefore not occur under atmospheric conditions. In the present work we have investigated the growth of $HCl \cdot 6H_2O$ on a thin ice film and find that it requires $T \leq 173$ K. The discussion will emphasize newer results (McNeill et al., 2006, 2007; Henson et al., 2007) published on or after 2006 given the review of Huthwelker et al. (2006) that provides an excellent summary of our state of knowledge on the HCl–H_2O system up to this date. However,

Table 1. Characteristic parameters of the stirred flow reactor (SFR).

Stirred-flow reactor volume V	HCl calibrated volume for inlet	H_2O calibrated volume for inlet	Si window area for deposition	MS calibration factor (H_2O) (A^{-1}molec s^{-1})	Escape rate constant k_{esc} across leak[b]	Gas–wall coll. freq. ω (s^{-1})[a,b] with Si window
2350 cm^3	60 cm^3	44 cm^3	0.78 cm^2 [a]	1.4 10^{24} (H_2O) 1.8 10^{24} (HCl)	0.055 (H_2O) 0.039 (HCl)	5.17 (H_2O) 3.66 (HCl)

[a] One-sided. [b] Values for k_{esc} and ω are valid for the chamber heated to 330 K.

we will occasionally revisit older studies in the discussion as well in order to support and interpret the present results.

2 Experimental

2.1 The reactor

The reactor (see Table 1) is identical to the one used by Delval (2003) apart from a number of improvements that are described in Supplement 1. In short, it consists of a high-vacuum chamber where deposition of a thin film takes place on a temperature-controlled Si substrate equipped with various diagnostics. A key feature of the reactor is the presence of a single cold point, namely the Si surface, where condensation of gases admitted into the chamber will occur and which affords a 1 : 1 correspondence between changes in the gas- and the condensed-phase composition.

2.2 Growth protocol for HCl · 6H$_2$O

The following protocol was developed in order to grow a pure crystalline HCl hexahydrate film (HCl · 6H_2O). First, a pure ice film of one to two micron (µm) thickness was grown by backfilling the chamber with bidistilled water vapor for a few minutes, at typical flow rates of 10^{16} molecules s^{-1}, with the Si optical support held at temperatures between 170 and 190 K. Due to the backfilling procedure in the static reactor, the film grew on both sides of the support. The sample was then exposed to HCl vapor by backfilling the chamber for a variable period of 1–2 min: this operation was performed under static – that is, no pumping – conditions at typical inlet flow rates of 10^{15} molecules s^{-1}. After each gas admission to the upper chamber it was briefly pumped for a few minutes in order to remove excess HCl or H_2O that had remained adsorbed to parts of the internal surface other than the optical Si window. This procedure was chosen as the latter is the only cold point in the chamber and the contribution of molecules evaporated from the film was negligible at 170 K. As an example, the temperature of the PTFE insulating the cryostat never decreased below 258 K when the Si window was kept at 170 K. After deposition of H_2O and HCl, the system was set to stirred-flow reactor (SFR) conditions by pumping through the calibrated leak. The temperature of the Si window was then gradually increased at a rate of approximately 1.5 K min^{-1} to the desired value around 187 K or above 190 K, as the case may be, constantly monitoring the change in composition of both the solid phase by means of FTIR absorption spectroscopy in transmission as well as of the gas phase by means of residual gas mass spectrometry (MS).

Two distinct solid phases have been obtained and studied, namely an amorphous and a crystalline structure, as a function of the pure ice film temperature at the moment of doping by a measured amount of HCl. For temperatures above 173 K the IR absorption spectra always showed features that could be attributed to an amorphous/supercooled (amHCl–H_2O) state. Moreover, attempts to crystallize the thin film starting from an amorphous sample by evaporating excess H_2O molecules and annealing the HCl–H_2O sample were unsuccessful for temperatures above 173 K. In contrast, for substrate temperatures below 173 K at the moment of doping, a new ordered phase attributed to the presence of HCl hexahydrate (HCl · 6H_2O, HH) was obtained, with the first characteristic IR absorption peaks visible within seconds after the start of doping with HCl.

3 Results and discussion

3.1 HCl hexahydrate growth and spectroscopic features

Ice deposited in the temperature range between 170 and 190 K at typical rates of 10^{16} molecules s^{-1} consists of polycrystalline I_h ice (Bergren et al., 1978). Sample thicknesses of films under study range from a few hundred nanometers to a few microns depending on the experiment. The main properties of pure ice films have been experimentally verified by measuring the H_2O equilibrium vapor pressure (P_{H_2O}) under static conditions and comparing it to the values available in the literature (Jancso et al., 1970; Marti and Mauersberger, 1993) in order to check the film temperature monitored by a type-T thermocouple. Subsequently, IR spectra were collected at different film thicknesses in order to measure the IR optical properties of the thin ice film: the cross section of the 3236 cm^{-1} peak was measured as $(8.0 \pm 0.8) \times 10^{-19}$ cm^2 by comparing the IR absorbance with the number of absorbers present in the solid phase. This was done

by completely desorbing the ice film and integrating the calibrated MS signal at m/e 18 in order to obtain the total number of H_2O molecules making up the ice film. These results are in agreement with Delval et al. (2003). The evaporation rate of pure ice was measured in the temperature range 173–190 K by means of the MS at high pumping speed (dynamic pumping), i.e., without H_2O condensation, and was found to be in agreement with Delval and Rossi (2004).

When a pure ice sample is exposed to backfilled HCl of a few tenths of mTorr at $T \leq 173$ K under static conditions, changes in the IR absorption spectrum of the film are immediately visible in the O–H stretch region (3000–3500 cm^{-1}), as displayed in Fig. 1, where traces *a* and *b* refer to pure ice and HCl-doped ice, respectively. The upper limit of the adsorbed HCl dose is 2.3×10^{17} molecules, corresponding to approximately 550 molecular monolayers (ML) adhering to each side of the 0.78 cm^2 Si window, where one monolayer corresponding to a consensus value of 2.7×10^{14} molecule cm^{-2} at 200 K (discussed below) compared to typically 3.1×10^{18} molecules of H_2O cm^{-2} for a 1 µm thick film corresponding to 3100 ML. The transition from trace *a* to *b* reveals a sudden decrease in the intensity of the peak at 3238 cm^{-1}, which corresponds to the O–H symmetric stretch for pure water ice, and the gradual appearance of two new peaks located at 3426 and 3365 cm^{-1}. Meanwhile, a less intense but very sharp peak at 1635 cm^{-1} starts to become visible that is associated with a bending mode of proton-ordered waters of hydration (Ritzhaupt and Devlin, 1991; Martin-Llorente et al., 2006). Characteristic peaks also appear in the regions between 1100 and 1300 cm^{-1} (mainly due to the $H_3O^+ \nu_2$ mode) and between 1700 and 2000 cm^{-1} (mainly due to the $H_3O^+ \nu_4$ mode). All of these features, listed in Table 2, are in agreement with those found in the literature (Graham and Roberts, 1995, 1997; Ritzhaupt and Devlin, 1991; Koehler et al., 1993) and are attributed to crystalline HCl · 6H$_2$O (HH).

Minor differences in the published spectra are detected in the O–H stretch region, where some groups (Ritzhaupt and Devlin, 1991) have identified four distinct peaks, while others (Graham and Roberts, 1997; Koehler et al., 1993) have found three, as we have in the present study. In the present work, the doping with HCl is performed directly onto pure polycrystalline vapor-deposited ice in contrast to amorphous ice as in most of the previous studies. The first spectral changes occur instantly under the present experimental conditions as observed already during HCl backfilling. A temperature of $T \leq 173$ K is required for nucleation of crystalline HH, in agreement with previous studies except that HH nucleation also occurs on polycrystalline hexagonal ice I_h. It does therefore not seem to be necessary to start with pure amorphous ice at low temperature in order to obtain the formation of crystalline HCl · 6H$_2$O.

Delval et al. (2003) have obtained a HCl–H_2O crystalline structure similar to HCl · 6H$_2$O using the identical experimental apparatus. However, the doping was performed at

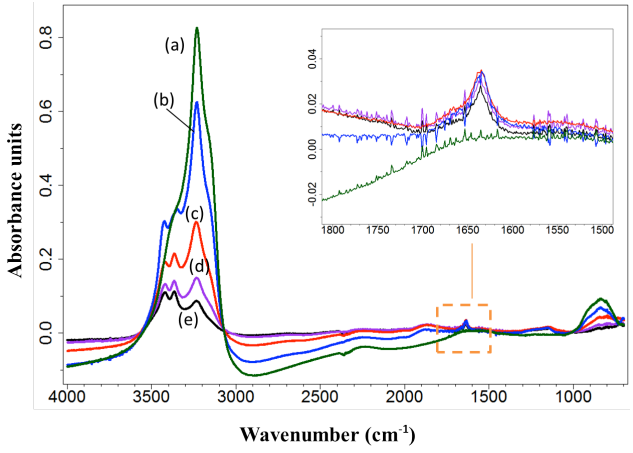

Fig. 1. IR transmission spectra of a pure ice film before **(a)** and after doping with gaseous HCl at 170 K at a typical dose of 1–2 $\times 10^{17}$ molecules. Spectra **(c)**, **(d)** and **(e)** have been collected in four scans each at 1 cm^{-1} resolution during film evaporation at increasing temperature under SFR (stirred flow) conditions. No offset has been introduced in order to facilitate the quantitative comparison between spectra.

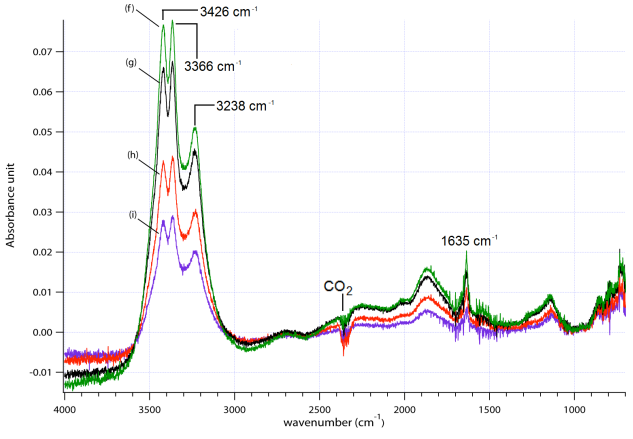

Fig. 2. IR spectra of the same ice–HCl film shown in Fig. 1 at successive stages during evaporation for 20 min at $T = 187 \pm 0.5$ K under SFR conditions. No offset has been introduced.

190 K at higher HCl partial pressure by HCl injection across a dosing tube that was tightly connected to the housing of the Si window rather than by HCl backfilling. The FTIR spectrum obtained by Delval et al. (2003) seems to be either a superposition of HCl · 6H$_2$O (HH) with an unknown ordered phase or two modifications of HH. Its FTIR absorption spectrum shows an additional OH stretch at 3549 cm^{-1} as well as a doublet at 1644 and 1618 cm^{-1} that probably stems from splitting of the 1635 cm^{-1} absorption band displayed in Table 3 and Fig. 2.

When the sample temperature is gradually raised under slow pumping (SFR) conditions across the bypass valve at a pumping speed for H_2O of $k_{esc}\, V = 0.13$ L s^{-1} (Table 1) in

Table 2. Principal peak positions in wave numbers (cm^{-1}) for the HCl · 6H$_2$O IR absorption spectrum and its spectroscopic assignments.

Type of vibration	Graham and Roberts (1997)	Ritzhaupt and Devlin (1991)	Abbatt et al. (1992)[a]	Delval et al. (2003)	This work[b]
Water H$_2$O ν_3	3399	3424	3437	3549, 3471	3426
		3375		3409	
Water H$_2$O $\nu_3 + \nu_1$	3353	3349	3381		3366
Water H$_2$O $\nu_3 + \nu_1$	3240	3235	3255	3264, 3244	3238
Oxonium ion ν_1	2701	2695	2703		2675
Oxonium ion ν_3	2337	2298	2262		2250
Oxonium ion ν_4	1931	1892	1850		1870
Bending vibration of the proton-ordered waters of hydration	1636	1635	1643	1644, 1618	1635
	1263	1278	1260		1286
Oxonium ion ν_2	1151	1147	1146		1138

[a] Estimated uncertainty in peak position of $\pm 12\,\mathrm{cm}^{-1}$, [b] estimated uncertainty in peak position of $\pm 2\,\mathrm{cm}^{-1}$.

Table 3. Measured differential absorption cross sections at different frequencies for a pure HCl hexahydrate film in the range 182 to 188 K*.

Wave number (cm^{-1})	Cross section per hexahydrate formula unit (cm^2 molec^{-1})
1635	$(6.5 \pm 1.9)\ 10^{-19}$
3238	$(1.4 \pm 0.4)\ 10^{-18}$
3426	$(2.3 \pm 0.7)\ 10^{-18}$

* The measured differential peak absorption cross section for pure vapor-phase deposited ice at 3236 cm^{-1} is (8.0 ± 0.8) 10^{-19} cm^2 molecule^{-1}.

order to allow evaporation of the film, these new IR absorption peaks become more distinct, while the total absorbance at 3000 cm^{-1} decreases as a consequence of the evaporation of H$_2$O. From the observation of the MS signals at m/e 18 (H$_2$O$^+$) and 36 (HCl$^+$) we are able to monitor the number of evaporated H$_2$O and HCl molecules that escape through the calibrated leak into the detection chamber (MS). The film is initially mostly undergoing selective evaporation of excess water that is not bound to HCl, thereby enriching the film in HH units. We note that the evaporation of H$_2$O initially takes place at a rate characteristic of pure ice (Delval and Rossi, 2005) despite the presence of crystalline HH on the ice substrate. At the same time, diffusion of HCl from the interface into the film may further contribute to crystallization of additional HH (Uras-Aytemiz, 2001). We point out that the HH spectra displayed in Fig. 2 are the only spectra corresponding to pure HH after evaporation of excess H$_2$O compared to all other HH spectra found in the literature.

The absorbance decrease in the 3000–3500 cm^{-1} region upon H$_2$O evaporation is stronger for the 3238 cm^{-1} (red) peak relative to the two neighboring (blue) peaks at 3426 and at 3365 cm^{-1}, and as a result the intensity of the red absorption band finally decreases in amplitude below the latter two. Changes in the overall shape of the IR spectrum occur only at the beginning of the evaporation of the sample. After a certain time, the overall shape of the IR absorption spectrum given by the peak ratios does not change as the film evaporates (see Fig. 2). We take this as an indication that a pure phase of constant composition has been obtained once the shape of the IR absorption spectrum ceases to change. In particular, the ratio of the absorbance of the peaks at 3426 to 3238 cm^{-1} (I_{3426}/I_{3238}) and 3365 to 3238 cm^{-1} (I_{3365}/I_{3238}) decreases from the initial value less than 1 to a constant value of approximately 1.6, which is constant until the end of evaporation. We therefore assume that we are in the presence of a stoichiometrically defined film of HCl · 6H$_2$O whose spectrum is time invariant. The FTIR transmission measurement is thus suitable to determine the defined stoichiometry of the sample, whereas the shape of the IR bands in reflection–absorption at grazing incidence (RAIRS) (Ortega et al., 2004, 2005, 2006; Graham and Roberts, 1995, 1997) strongly depends on the sample thickness and optical constants of the ice film. A small change in total sample thickness will strongly influence the RAIRS spectrum, even when the film is not undergoing any change in its composition.

The growth of HCl · 6H$_2$O film at $T \leq 173$ K under static conditions (backfilling) occurs in the presence of pure ice. Continued doping of a H$_2$O/HH film with HCl did not lead to quantitative conversion of the film into crystalline HCl · 6H$_2$O but led to the decay of the crystalline film to an amorphous phase, characterized by a heavily distorted IR spectrum (see below) at temperatures where HCl · 6H$_2$O was stable. This may be explained by the fact that the diffusion of HCl across the crystalline HCl · 6H$_2$O layer is the rate-limiting step in the continuing conversion of ice to HH

(Uras-Aytemiz, 2001) after initial formation of a HCl · 6H$_2$O crystalline layer on top of the film. This HCl diffusion across the initial crystalline HCl · 6H$_2$O layer is a temperature-dependent process. Bournel et al. (2002) found the temperature threshold at $T = 120$ K using both bulk- and surface-sensitive variants of NEXAFS for the HCl–H$_2$O system and attributed it to diffusion of HCl across pure H$_2$O/water ice. If HCl is available in excess under the present conditions, it accumulates in the uppermost layer of the film, causing the nucleation of an amorphous, liquid-like phase. Vuillard (1957) also reported on long times needed for bulk HCl · 6H$_2$O to reach equilibrium. Finally, we would like to emphasize that HCl present in the condensed phase, either as crystalline HCl · 6H$_2$O or amorphous HCl–H$_2$O phase, is electrolytically dissociated into H$_3$O · nH$_2$O$^+$Cl$^-$ complexes for $T \geq 90$ K. The result of this pioneering study by Parent and Laffon (2005) was obtained in NEXAFS investigations in the HCl–H$_2$O system using Cl and O atomic levels using both surface- and bulk-sensitive detection of electrons and ions at $T = 20$ and 90 K. It may be added that the OH-dangling bonds do not play a dominant role in HCl adsorption. The interaction of HCl with ice rather occurs by the initial perturbation of the surface and bulk ice crystalline ice structure driven by the thermodynamics of HCl dissolution.

3.2 HCl hexahydrate IR cross sections

In order to determine the IR absorption cross section of pure HCl · 6H$_2$O, we started the measurement after evaporation of excess H$_2$O in the HCl–H$_2$O binary system and once the shape of the IR absorption spectrum had ceased to change (Fig. 1e). After HCl doping, film thicknesses typically decreased from initially 1 to 2 µm to approximately 400 to 800 nm after excess H$_2$O evaporation. Thereafter, we periodically collected IR spectra of pure HH during its evaporation in the vicinity of typically 190 K and compared the IR absorbance to the total number of water molecules in the condensed phase by desorbing the film.

The total number of water molecules of evaporating HCl · 6H$_2$O is determined by using a calibrated MS signal I^{18} at m/e 18. As there is only one cold spot in the reactor, namely the Si substrate for the film, we are confident that the latter is the only source of gas-phase H$_2$O. Thus, we obtain the absolute rate of H$_2$O evaporation in molecules per second by analyzing the calibrated MS signal I^{18} during evaporation of the film. Upon integration of I^{18} over time we find the total number of molecules N_{tot} that evaporated from the film after a given time:

$$N_{\mathrm{tot}} = \int I_{18}(\tau)\mathrm{d}\tau. \quad (1)$$

Using a mass balance argument for H$_2$O we calculate the number of molecules $N^{\mathrm{cond}}_{\mathrm{H_2O}}$ still present in the condensed phase at time t from the beginning of the experiment at t_0:

$$N^{\mathrm{cond}}_{\mathrm{H_2O}}(t) = N_{\mathrm{tot}} - \int_{t_0}^{t} I_{18}(\tau)\mathrm{d}\tau. \quad (2)$$

In a similar fashion, we may relate the IR absorbance of H$_2$O–ice to the column density of a HCl · 6H$_2$O film. We have assumed a 6 : 1 composition of H$_2$O to HCl consistent with the spectroscopic assignment because we were unable to quantitatively determine the amount of HCl adsorbed on ice using the MS signal at $m/e = 36$ owing to HCl adsorption on the walls of the SFR. We have therefore inferred the 6 : 1 H$_2$O : HCl stoichiometry from a MS spectroscopic measurement of the number of condensed H$_2$O molecules in the HH film given that the HH spectral signature in the IR had already been well established in previous studies (Ritzhaupt and Devlin, 1991; Delzeit et al., 1993; Koehler et al., 1993; Graham and Roberts, 1995, 1997). In subsequent work we have experimentally determined the amount of HCl in these ice films using mass balance coupled to the HCl adsorption isotherm for HCl interacting with the internal surface of the SFR (Iannarelli and Rossi, 2013).

The relationship between the absorbance and the number concentration of HH units is linear according to the Beer-Lambert law following Eq. (3):

$$I(\lambda) = I_0(\lambda)e^{-n\sigma(\lambda)d}, \quad (3)$$

where I_0 and I are the IR beam intensities before and after passage through the sample, respectively, λ is the wavelength, n is the concentration in molec cm^{-3}, $\sigma(\lambda)$ is the differential IR absorption cross section in cm^2 molec^{-1} at wavelength λ and d is the sample thickness in cm. By plotting 2.303 times the absorbance, $\log\left[I_0(\lambda)/I(\lambda)\right]$, as a function of nd, the numerical value of $\sigma(\lambda)$ will be given by the slope of the fitted line (Fig. 3). A 30 % overall uncertainty in σ is attributed mainly to the measurement of the HH concentration. In Table 3, differential IR absorption cross sections are given for different wave numbers in terms of HH units.

From the data of Koehler et al. (1993) we calculate a peak differential IR absorption cross section of 5.6×10^{-19} cm^2 molec^{-1} at 1635 cm^{-1} using the measured optical density of 0.095 at 1635 cm^{-1} across a HCl-doped 900 nm thick ice deposit and making the assumption that each formula unit of HCl · 6H$_2$O comprises seven molecules out of the doped ice film. This number compares favorably with $\sigma = (6.5 \pm 1.9) \times 10^{-19}$ cm^2 molec^{-1} measured in this work at 1635 cm^{-1}. The integration of the differential IR absorption cross section from 1621 to 1657 cm^{-1} obtains an estimate of the integral IR absorption cross section of 1.4×10^{-20} cm^2 molecule^{-1} using a full width half maximum bandwidth of 33 cm^{-1} centered at 1635 ± 2 cm^{-1}. We compare the intensity of the antisymmetric O–H stretch vibration ν_3, which is the most intense of all three fundamental vibrations at 3426 cm^{-1} for pure HCl · 6H$_2$O with

Table 4. Mass balance considerations. Comparison between the dispensed HCl dose obtained from the pressure decrease in the calibrated volume, the HCl dose calculated from the change in the IR spectrum and the HCl dose present when a pure HCl · 6H$_2$O film is formed assuming a 6 : 1 H$_2$O to HCl composition.

Sample number[a]	Upper limit HCl dose from $\Delta P(HCl)_{cal.volume}$ (molec)	ΔA (absorbance change) upon HCl doping	HCl dose from ΔA (molec) (molec)	Fractional loss of HCl[b] from ΔA	HCl dose present in the pure HCl · 6H$_2$O (molec)	Fractional loss of HCl[c] from H$_2$O count
1	1.1×10^{17}	0.16	9.0×10^{16}	0.182	7.0×10^{16}	0.364
2	2.1×10^{17}	0.20	1.1×10^{17}	0.476	5.0×10^{16}	0.762
3[d]	1.3×10^{17}	0.25	1.4×10^{17}	< 0	1.2×10^{17}	0.077
4	2.0×10^{17}	0.23	1.3×10^{17}	0.350	1.3×10^{17}	0.350
5	2.1×10^{17}	0.23	1.3×10^{17}	0.381	1.5×10^{17}	0.286
6	2.3×10^{17}	0.23	1.3×10^{17}	0.435	1.4×10^{17}	0.304

[a] Sample numbers refer to the same experimental run as in Table A2.2 in Supplement 2 and Fig. 3.
[b] Fractional loss of HCl by comparing measured dose (first column) with HH based on A and IR absorption cross section obtained in this work. Average value (excluding sample no. 3): 0.365 ± 0.113.
[c] Fractional loss of HCl by comparing measured dose (first column) with HH based on counting 1/6 the number of H$_2$O molecules evaporating from pure HH using calibrated mass spectrometry (m/e 18). Average value (excluding sample no. 3): 0.413 ± 0.177.
[d] Regarded as an outlier.

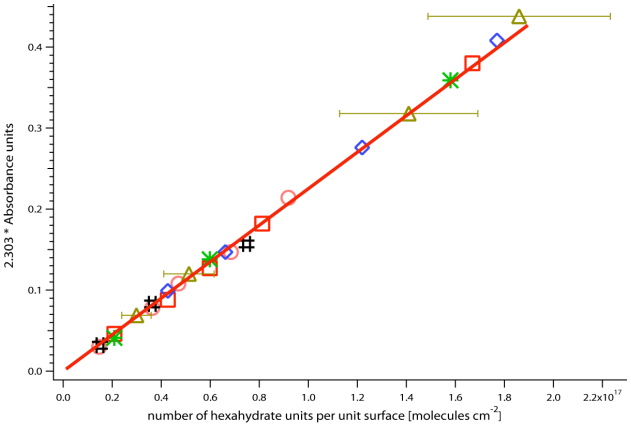

Fig. 3. Plot of the IR absorbance at 3426 cm^{-1} as a function of the number of formula units per unit surface for pure HCl hexahydrate (HCl · 6H$_2$O). The different symbols represent the six different samples listed in Table 3. From the fit one obtains a cross section of $\sigma = (2.3 \pm 0.7)\ 10^{-18}$ cm^2 molec^{-1} per HCl hexahydrate formula unit.

3236 cm^{-1} for pure ice. In fact, the σ value for pure HCl · 6H$_2$O at 3426 cm^{-1} from Table 3 is a factor of 2.087 smaller than one-sixth the value of σ for pure ice at its peak of 3236 cm^{-1}. This decrease in absorption strength in the 3000 cm^{-1} region is clearly visible at the start of HCl doping of a pure ice film at HH growth conditions ($T \leq 173$ K) as may be seen in Fig. 1 for spectrum a and b taken about 1–2 min apart in consecutive FTIR scans.

In Table 4 we present data for the experiments displayed in Fig. 3 and Table A2.2 in Supplement 2 in order to bracket the HCl content of doped ice using mass balance arguments. An upper limit for the dispensed HCl dose upon admission to the reactor has been obtained by monitoring the decrease in the HCl partial pressure in a calibrated volume and is displayed in the second column of Table 4. The actual dose deposited on the ice film may be lower as not every admitted HCl molecule may lead to crystalline HCl · 6H$_2$O in the presence of excess H$_2$O in the film. Typical upper limits are on the order of $(1.0\text{–}2.0) \times 10^{17}$ molecules. Smaller values for the amount of HCl present in the film are found when considering the difference in absorbance (OD) immediately before and after the exposure to HCl using the cross sections for pure ice and HH at 3236 and 3238 cm^{-1}, respectively. In this case we obtain a typical HCl range of $(0.9\text{–}1.4) \times 10^{17}$ molecules as displayed in the fourth column of Table 4 and corresponds to an average of 0.365 ± 0.113 of the dosed HCl (second column). The typical amount of HCl at the start of a pure HH (without excess H$_2$O) evaporation experiment is obtained by taking one-sixth of the integrated number of evaporating H$_2$O using calibrated MS intensities. This leads to approximately $(0.5\text{–}1.5) \times 10^{17}$ HCl molecules shown in the sixth column of Table 4, which corresponds to 0.413 ± 0.177 of dosed HCl displayed in the second column. This implies that part of the initially admitted HCl ended up as adsorbate on the internal walls (stainless steel) of the SFR, in agreement with the HCl adsorption isotherm for the SFR chamber (Iannarelli et al., 2013) when we compare the second and sixth or second and fourth columns of Table 4. For the calculation of the IR absorption cross sections the HCl concentration values in the sixth column of Table 4 have been used.

3.3 HCl hexahydrate kinetic and thermodynamic properties

We have taken the MS signal of H$_2$O at m/e 18 under SFR conditions, which is proportional to the net evaporation rate $R_{ev}{}^{net}$ molec cm^{-3} s^{-1}, and related it to the equilibrium partial pressure of H$_2$O in the chamber, $P_{eq}(H_2O)$. SFR conditions lead to a net evaporation rate because the H$_2$O condensation rate constant is significant compared to the (slow)

pumping rate constant $k_{esc}V = 130\,cm^3\,s^{-1}$ (Table 1) across the leak. The relationship between the absolute (R_{ev}) and net rate of H_2O evaporation ($R_{ev}{}^{net}$) in the presence of ice is given in Eq. (4):

$$R_{ev}{}^{net} = R_{ev} - k_{cond}[H_2O]_{ss}, \quad (4)$$

where $R_{ev}{}^{net}$ and R_{ev} are the net and the absolute H_2O evaporation rates, respectively, in molec s^{-1} cm^{-3}, k_{cond} is the condensation rate constant in s^{-1} and $[H_2O]_{ss}$ corresponds to the partial pressure of water in the reactor under SFR (= steady-state) conditions in molec cm^{-3}. It turns out that we are operating close to equilibrium at typical experimental conditions from 185 to 195 K. This is primarily due to the small escape rate constant across the leak (k_{esc}/s^{-1}), but also due to the low value of R_{ev} owing to the low substrate temperature, which renders evaporation and condensation rates competitive. The equation that relates the equilibrium water vapor pressure $P_{eq}(H_2O)$ to its steady-state value at stirred-flow conditions, $P_{ss}(H_2O)$, is given in Eq. (5):

$$P_{eq}(H_2O) = P_{ss}(H_2O)(1 + k_{esc}/k_{cond}). \quad (5)$$

Using $k_{esc} = 0.055\,s^{-1}$ and $k_{cond} = 1.0\,s^{-1}$ at 193 K for H_2O on pure (C) ice condensed from the vapor phase (Delval et al., 2003), P_{eq} is only 5.5 % higher than the measured P_{ss}, which is a small correction for P_{ss} (H_2O) given the uncertainty in the measurements. However, for an ice surface doped with HCl, k_{cond} is significantly smaller according to Delval et al. (2003). Although we have not measured k_{cond} in the present work, we estimate that at 193 K, k_{cond} is a factor of five smaller for HCl–H_2O ice compared to pure ice in analogy to results obtained in the H_2O / HCl system by Delval et al. (2003). We obtain $k_{cond} = 1.0/5 = 0.20\,s^{-1}$ for the HCl-containing system and therefore apply the correction factor $P_{eq}/P_{ss} = 1.281$ to the SFR data.

According to the HCl–H_2O phase diagram (Hanson and Mauersberger, 1990; Molina, 1994; McNeill et al., 2006) the experimental results point to the existence of HH ($HCl \cdot 6H_2O$) with variable amounts of ice according to the measured partial pressures of both HCl and H_2O. Of special interest are the conditions where the system finds itself on one of the coexistence lines with respect to the relevant phases, namely ice/HH or HH/HCl trihydrate (TH). For the former, the dependence of the vapor pressure of HCl, P_{eq}(HCl), on the temperature is given in Eq. (6), whereas $P_{eq}(H_2O)$ is given by pure ice because both phases, namely pure ice and HH/ice, share a common value of the H_2O vapor pressure $P_{eq}(H_2O)$.

$$\begin{aligned} d\ln P_{eq}(HCl)/d(1/T) &= (6\Delta H^0_{sub,ice} - \Delta H^0_{sub,HH})/R \quad (6)\\ &= -65820/R(Jmol^{-1}K^{-1}), \end{aligned}$$

where $\Delta H^0_{sub,ice} = 50.93$ and $\Delta H^0_{sub,HH} = 371.40\,kJ\,mol^{-1}$ are the standard enthalpies of sublimation of ice and HH at 200 K given by Wooldridge et al. (1995). For the coexistence of HH and TH, the corresponding equations for the temperature dependence of both $P_{eq}(H_2O)$ and P_{eq}(HCl) are given in Eqs. (7) and (8). In this case the vapor pressure of H_2O is lower than that of pure ice because $P_{eq}(H_2O)$ is shared between HH and TH.

$$\begin{aligned} d\ln P_{eq}(H_2O)/d(1/T) &= (\Delta H^0_{sub,TH} - \Delta H^0_{sub,HH})/(-3R)\\ &= 54733/R(Jmol^{-1}K^{-1}), \quad (7)\\ d\ln P_{eq}(HCl)/d(1/T) &= (6\Delta H^0_{sub,TH} - 3\Delta H^0_{sub,HH})/\\ &(3-6)R = -43000/R(Jmol^{-1}K^{-1}), \quad (8) \end{aligned}$$

where $\Delta H^0_{sub,TH} = 207.20\,kJ\,mol^{-1}$ is the standard heat of sublimation for TH. Wooldridge et al. (1995) gave an accurate estimate of the basic thermodynamic parameters needed for the calculation of the temperature dependence of both H_2O and HCl in the presence of HH and TH. In applying Eqs. (6), (7) and (8) it is important to recognize that "sublimation" in relation to $\Delta H^0_{sub,TH}$ and $\Delta H^0_{sub,HH}$ refers to the hypothetical phase transition of *all* components, namely H_2O and HCl, whereas HCl sublimation from $HCl \cdot 3H_2O$ and $HCl \cdot 6H_2O$ alone requires only 54.7 and 65.8 $kJ\,mol^{-1}$, respectively, when H_2O is left behind as crystalline water ice.

We note that $P_{eq}(H_2O)$ of a mixture of pure ice and HH, so-called H_2O-rich HH, where some excess H_2O is still present, is that of pure ice. After evaporation of excess water, $P_{eq}(H_2O)$ over pure HH is identical within experimental uncertainty to pure ice once $P_{ss}(H_2O)$ has been multiplied by 1.28 in order to obtain $P_{eq}(H_2O)$ (see above). Figure A2.1 in Supplement 2 displays a summary of $P_{eq}(H_2O)$ based on measured values of $P_{ss}(H_2O)$ above $HCl \cdot 6H_2O$ over a narrow temperature range of 7 K. This range is narrow because at $T > 195$ K the decay of the crystalline HH structure owing to thermal decomposition prevents measurements at higher temperatures (see Sect. 5.3), while at $T < 185$ K, R^{ev}_{net} (Eq. 4) becomes immeasurably small. Values for $P_{eq}(H_2O)$ for pure ice were set numerically equal to steady-state H_2O pressures ($P_{ss}(H_2O)$) because the correction according to Eq. (5) only amounted to an upward scaling by 5.5 %. However, we have chosen to apply the correction factor of 1.281 to $P_{ss}(H_2O)$ for ice doped with HCl (see above).

Figure A2.2 displays a van't Hoff plot of $P_{eq}(H_2O)$ over $HCl \cdot 6H_2O$ in coexistence with H_2O ice. Equation (10) predicts a reaction enthalpy corresponding to the difference between the heats of sublimation for HH and TH of 54.8 $kJ\,mol^{-1}$ as opposed to 51.0 $kJ\,mol^{-1}$ for the coexistence of ice with HH. From the slope of the fitted line in Fig. A2.2 we obtain an enthalpy of sublimation $\Delta H^0_{sub}(H_2O) = 55.7 \pm 10.5\,kJ\,mol^{-1}$ when we discard the outlier at 188 K (low value). Very clearly, the precision of the present temperature-dependent data of $P_{ss}(H_2O)$ does not allow for a choice to be made between the two coexistence lines owing to the experimental uncertainty due to too narrow a temperature range. However, the absolute values displayed in Fig. A2.1 suggest a value of $P_{eq}(H_2O)$ identical to pure

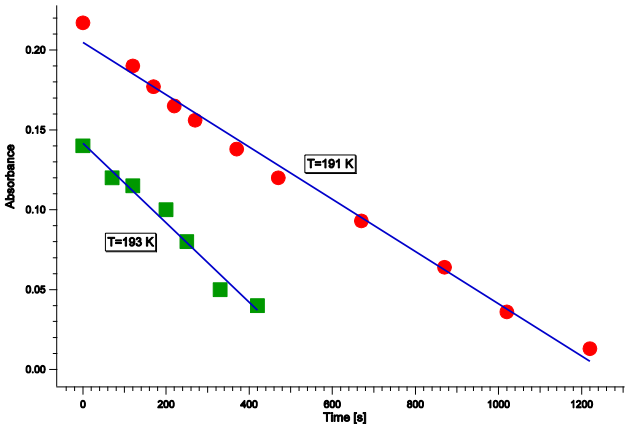

Fig. 4. Rate of decrease of IR absorbance at 3426 cm^{-1} of a pure HCl · 6H$_2$O sample during evaporation under SFR conditions at $T = 191$ and 193 ± 1 K displayed as a function of time. See also Fig. 2.

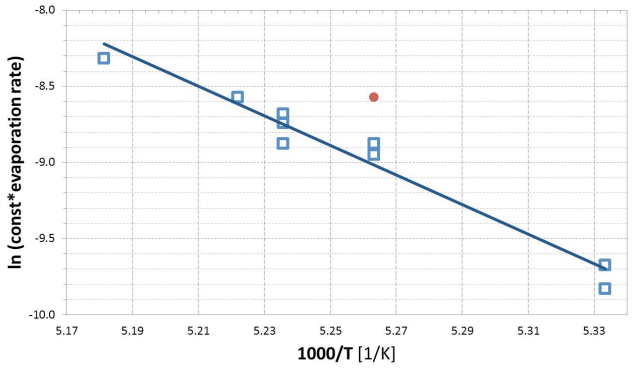

Fig. 5. Arrhenius plot of the rate of change of the IR absorption of pure HCl · 6H$_2$O. From the slope ($m = -9722$), one obtains the activation energy E_a for HCl sublimation in HCl · 6H$_2$O of 80.8 ± 5.8 kJ mol^{-1} leading to $\log J_{ev}$/molec cm^{-2} s^{-1} = $(36.3 \pm 3.2) - (80.8 \pm 5.8)/2.303RT$; $R = 8.314$ JK^{-1}mol^{-1} without taking into account the outlier (red circle). The evaporation rate of HCl has been multiplied by log(e) $\sigma(3426\,\mathrm{m}^{-1}) = 1.0 \times 10^{20}$ cm^2 molec^{-1} (ordinate).

ice within experimental uncertainty corresponding to the ice–HH coexistence. In practice, all possible values of $P_{eq}(H_2O)$ between the two coexistence values may occur depending on the chemical composition of the solid phase.

The multidiagnostic nature of the present experiment offers the opportunity to measure the decay of the optical density of HH under SFR conditions. In fact, by monitoring the decrease in the IR absorbance as a function of time at different IR absorption peaks of pure HCl · 6H$_2$O during its evaporation, we have a measure of the number of H$_2$O and HCl molecules evaporated from the solid phase. Results from two typical experiments are presented in Fig. 4 following the rate of change of the IR absorption peak at 3426 cm^{-1}. The evaporation takes place at a constant temperature of 191 and 193 K, and except for minor oscillations attributable to small variations in temperature, a linear decrease of absorbance with time is observed. This indicates a zero-order rate law, usually characteristic of the evaporation kinetics of a pure bulk phase. The slope at different temperatures in the range 187.5–193 K is plotted in Arrhenius fashion in Fig. 5 and summarized in Table 5.

The change in optical density A (absorbance) at a given characteristic peak of HH, for example at 3426 cm^{-1}, is given in Eq. (9) as follows:

$$2.303\Delta A = n\sigma^{HH}\mathrm{d}/\mathrm{d}t(<\mathrm{d}>) = \sigma^{HH}J_{ev}(\mathrm{HCl}), \quad (9)$$

where n, σ^{HH}, $<\mathrm{d}>$ and J_{ev} are the number density (molecule cm^{-3}), the differential absorption cross section at wavelength λ (cm^2 molec^{-1}), the optical pathlength (cm) and the evaporation flux (molec s^{-1} cm^{-2}) of HCl, respectively. The decay of A corresponds to Reaction (R4), which describes the sublimation of HCl from HCl · 6H$_2$O with $\Delta H^0_{sub} = 65.4$ and 65.8 kJ mol^{-1} at 300 and 200 K, respectively, according to Wooldridge et al. (1995):

$$\mathrm{HCl{\cdot}6H_2O}(s) \rightarrow 6\mathrm{H_2O}(s) + \mathrm{HCl}(g) \quad (R4)$$

Thibert and Dominé (1997) find a value of $\Delta h^s_{HCl} = 63.7 \pm 7.6$ kJ mol^{-1} that they call "partial enthalpy of HCl sublimation", which is identical within experimental uncertainty to the Wooldridge et al. (1995) value and pertains to Reaction (R4). This process does not correspond to true sublimation because water remains in the condensed phase. The release of HCl upon evaporation cannot lead to regeneration of crystalline HCl · 6H$_2$O and corresponds to a spontaneous irreversible process at $T \geq 173$ K in agreement with its growth conditions at $T \leq 173$ K. The spontaneous HH decay according to Reaction (R4) is induced by HCl evaporation as the rate-limiting step and the failure to nucleate HH, and is thus responsible for the phase transition of crystalline HCl · 6H$_2$O to a metastable amorphous/supercooled HCl–H$_2$O phase (amHCl–H$_2$O).

Table 5 lists the obtained values of J_{ev}(HCl · 6H$_2$O)/molec cm^{-2} s^{-1} using σ^{HH} of 2.3×10^{-18} cm^2 molec^{-1} at 3426 cm^{-1} that are plotted in Fig. 5 in Arrhenius fashion, resulting in a HCl evaporation flux given in Eq. (10):

$$\log J_{ev}(\mathrm{HCl{\cdot}6H_2O}) = (36.34 \pm 3.20) - (80\,810 \pm 5800)/2.303\,RT,\ R = 8.314\mathrm{JK^{-1}mol^{-1}}, \quad (10)$$

with an activation energy $E_a = 80.8 \pm 5.8$ kJ mol^{-1}. This analysis excludes an outlier at 190 K, as indicated in Table 5. Despite the small temperature range of 5.5 K, the data reveal a significant T dependence, as may be seen from Fig. 5.

Table 5. Rate of decrease of absorbance upon evaporation of a HCl • 6H$_2$O film at different temperatures in comparison with net evaporation ration rates for pure ice together with evaporation rates for ice and HCl hexahydrate.

T/K	$-dA/dt$ (s^{-1}) (absorbance change with time)	J_{ev}(HCl • 6H$_2$O)[a] (molec cm^{-2} s^{-1}) equals J_{ev}(HCl)	J_{ev}^{net}(H$_2$O) (molec cm^{-2} s^{-1}) (pure ice)	J_{ev}(H$_2$O)[b] (molec cm^{-2} s^{-1})	Ratio r of net evaporation rates[c]	ln r
187.5	6.3×10^{-5}	6.3×10^{13}	7.7×10^{14}	1.45×10^{16}	12.22	2.503
187.5	5.4×10^{-5}	5.4×10^{13}	7.7×10^{14}	1.45×10^{16}	14.26	2.657
190	1.4×10^{-4}	1.4×10^{14}	1.2×10^{15}	2.26×10^{16}	8.57	2.148
190[d]	1.9×10^{-4}	1.9×10^{14}	1.2×10^{15}	2.26×10^{16}	6.32	1.843
190	1.3×10^{-4}	1.3×10^{14}	1.2×10^{15}	2.26×10^{16}	9.23	2.223
191	1.6×10^{-4}	1.6×10^{14}	1.4×10^{15}	2.63×10^{16}	8.75	2.169
191	1.7×10^{-4}	1.7×10^{14}	1.4×10^{15}	2.63×10^{16}	8.23	2.108
191	1.4×10^{-4}	1.4×10^{14}	1.4×10^{15}	2.63×10^{16}	10.00	2.303
191.5	1.9×10^{-4}	1.9×10^{14}	1.5×10^{15}	2.82×10^{16}	7.89	2.066
193	2.45×10^{-4}	2.45×10^{14}	2.0×10^{15}	3.76×10^{16}	8.16	2.100

[a] From slope m of Fig. 5 using $m = 0.4343\,\sigma(3426\ cm^{-1}) \cdot J_{ev}$(HCl • 6H$_2$O) with $\sigma = 2.3 \cdot 10^{-18}$ cm^2 molec^{-1}. [b] J_{ev}(H$_2$O) = 18.82 J_{ev}^{net}(H$_2$O) (see text) [c] The ratio r is defined as $r = J_{ev}^{net}$ (H$_2$O) / J_{ev}(HCl • 6H$_2$O). [d] Outlier, not included in least-squares regression.

Figure 6 displays an alternative approach that shows an Arrhenius plot of the ratio r vs. $1/T$. The ratio r is defined as $r = J_{ev}^{net}(H_2O) / J_{ev}(HCl \cdot 6H_2O)$ and describes the relative change in the evaporation rates referenced to pure ice (Pratte et al., 2006). Figure 6 reveals an activation energy $E_a = -29.5 \pm 9.6$ kJ mol^{-1} that, taken together with E_{ev} (H$_2$O) $= 49.8 \pm 5.4$ kJ mol^{-1}, results in an absolute value of $E_a = 49.8 + 29.5 = 79.3 \pm 11.1$ kJ mol^{-1}. This value for E_a relative to the evaporation kinetics of pure ice is identical within experimental error to the absolute value of $E_a = 80.8 \pm 5.8$ kJ mol^{-1} obtained from the decay of the FTIR absorption (Arrhenius plot of Fig. 5). The two data treatments lead to results that are identical within experimental uncertainty despite the narrow temperature range.

Table 5 displays the evaporation flux J_{ev}(HCl • 6H$_2$O) in molecular units resulting from the decay kinetics of the IR absorption band at 3426 cm^{-1}. In order to compare J_{ev}(HCl • 6H$_2$O) $= J_{ev}$(HCl) with the corresponding value for pure ice we have to convert $R_{ev}{}^{net}$ or J_{ev}^{net} from Eq. (4) to their absolute values R_{ev} and J_{ev}. We calculate R_{ev} using $k_{cond} = 1.0\ s^{-1}$ for pure ice at 193 K (Delval et al., 2003) according to Eq. (11) and take note that the ratio of the evaporation flux is identical to the H$_2$O evaporation rate ratio: $J_{ev} / J_{ev}^{net} = R_{ev} / R_{ev}{}^{net}$:

$$R_{ev} = R_{ev}{}^{net}(1 + k_{cond}/k_{esc}), \quad (11)$$

Using the numerical values mentioned above for k_{esc} and k_{cond} we obtain $J_{ev} / J_{ev}^{net} = 18.82$ for H$_2$O evaporating from pure H$_2$O ice. These values are displayed in the fifth column of Table 5 (J_{ev}(H$_2$O)). We believe that the above correction factor for the conversion of J_{ev}^{net}(H$_2$O) to J_{ev}(H$_2$O) will not significantly change over the narrow temperature range of the present study because neither k_{esc} nor k_{cond} significantly change over $\Delta T = 5.5$ K (Table 5). Figure 7 displays

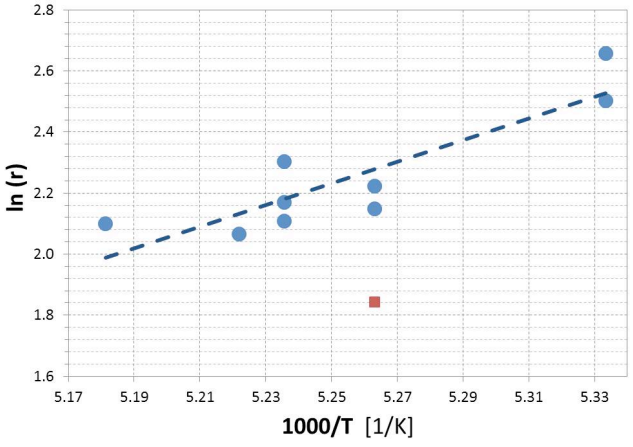

Fig. 6. Arrhenius plot of r corresponding to $r = J_{ev}^{net}$ (H$_2$O) / J_{ev}(HCl • 6H$_2$O) leading to a slope of 3544.7 corresponding to E_a^{sub}(H$_2$O)$-E_a^{sub}$(HCl • 6H$_2$O) $= -29.5 \pm 9.6$ kJ mol^{-1}. The slope has been evaluated without taking into account the outlier (red square).

the HCl evaporation fluxes J_{ev}(HCl • 6H$_2$O) (this work) and J_{ev}(H$_2$O) for pure and HCl-doped ice leading to an amorphous phase (Delval et al., 2003) as well as J_{ev}(HCl) for HCl-doped amorphous phase ice in the relevant temperature and pressure range. Using the data of Flückiger et al. (1998) this HCl evaporation flux is given in Eq. (12):

$$\log J_{ev}(HCl) = (20.6 \pm 2.1) - (21967 \pm 4800)/2.303RT,$$
$$R = 8.314\,J\,K^{-1}mol^{-1}. \quad (12)$$

These evaporation fluxes are plotted as straight lines in the Arrhenius representation in Fig. 7 except for the break around 190 ± 2 K for pure ice, which has been described

by Chaix et al. (1998), Delval et al. (2004) and Pratte et al. (2006). J_{ev}(HCl) of this work pertaining to crystalline HCl · 6H$_2$O intersects the shallow line corresponding to J_{ev}(HCl) from an amorphous phase (quasi-liquid layer) at T =195 K (Flückiger et al., 1998) and thus follows the crystalline to amorphous phase change observed in the FTIR absorption spectra discussed below. Assuming that the purple line J_{ev}(HCl · 6H$_2$O) for HH decomposition through HCl evaporation is the rate-limiting step, the reaction path first follows the steep purple line starting at the low-temperature end up to T = 195 K. Subsequently, HCl evaporation from HH follows the shallow green line for T > 195 K upon phase change from crystalline HH to amHCl–H$_2$O (see below). Owing to the irreversible reaction (13) leading to gas-phase HCl, the inverse reaction cannot regenerate crystalline HCl · 6H$_2$O at this temperature but instead leads to adsorption of HCl on ice, resulting in an amorphous or "quasi-liquid layer" whose evaporation kinetics have a lower activation energy and is given in Eq. (12) above (Flückiger et al., 1998). Pure HCl · 6H$_2$O is stable at $T \leq 173$ K but irreversibly decomposes at T > 173 K. At this point the reader is reminded that the measured steady-state pressure of HCl and H$_2$O is only 5 % lower than its corresponding equilibrium values according to Eq. (5). Therefore, the present experimental conditions are close to equilibrium under SFR conditions.

We have the significant result that the activation energy $E_a = 80.8 \pm 5.8$ kJ mol^{-1} for HCl · 6H$_2$O evaporation, as observed from the decay kinetics of the IR absorption spectrum, is significantly larger than expected based on the thermodynamic value of $\Delta H^0_{sub,HH} = 65.4$ kJ mol^{-1} according to Reaction (R4). We expect that E_a for HCl condensation onto HCl · 6H$_2$O should be close to zero at 190 K or even slightly negative akin to HCl interacting with pure ice with E_a in the range -7.5 ± 1.3 to -13.0 ± 1.3 kJ mol^{-1} (Flückiger et al., 1998). However, the measured activation energy for HCl · 6H$_2$O thermal decomposition is larger than expected and implies that the inverse of Reaction (R4) will have a substantial intrinsic barrier of approximately 80.6–65.8 = 14.8 kJ mol^{-1} above and beyond the thermodynamic limit of 65.8 kJ mol^{-1} at 200 K. Figure 7 also shows that J_{ev} for HCl and H$_2$O are not comparable as J_{ev}(H$_2$O) is roughly two orders of magnitude or so larger than the corresponding J_{ev}(HCl) (Iannarelli and Rossi, 2013). This means that the rate-limiting step in HH decomposition is HCl evaporation according to Reaction (R4) and will remain so after phase transition from crystalline HH to amHCl–H$_2$O at T = 195 K because J_{ev}(HCl) for the amorphous phase displayed by the green line in Fig. 7 is lower than J_{ev}(H$_2$O) for pure ice after the "break" at $T > 193 \pm 2$ K (dashed blue line, Fig. 7 following data of Pratte et al., 2006). This turnover for HH occurs at or around 195 K when the reaction path changes from the purple (HH) to the green path (amHCl–H$_2$O) displayed in Fig. 7.

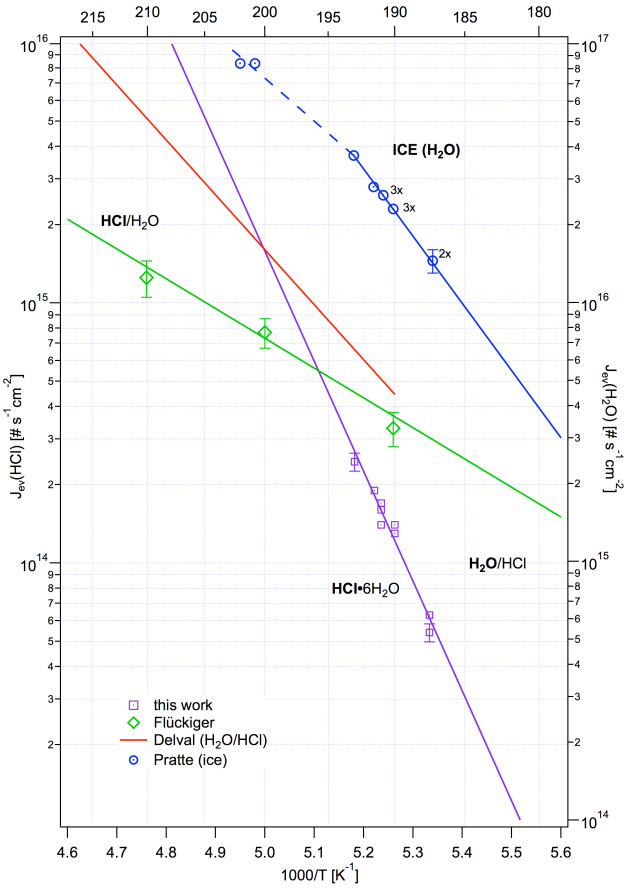

Fig. 7. HCl (left ordinate, bold HCl in plot) and H$_2$O (right ordinate, bold H$_2$O in plot) evaporation rates as a function of 1/T of HCl · 6H$_2$O (this work, decay monitored using FTIR absorption of HCl · 6H$_2$O, purple line), HCl–H$_2$O (Flückiger et al., 1998; green line), H$_2$O / HCl (Delval et al., 2003; red line) and pure H$_2$O ice (Pratte et al., 2006; blue line). The green and purple lines correspond to logJ_{ev}(HCl)/molec cm^{-2} s^{-1} = (20.6 ± 2.1) – (21 967 ± 4800)/2.303 RT, and logJ_{ev}(HH)/molec cm^{-2}s^{-1} = (36.34 ± 3.20) – (80 810 ± 5800)/2.303RT, R = 8.314 J K^{-1} mol, respectively.

3.4 Amorphous HCl–H$_2$O phase

When the exposure of a pure polycrystalline ice film to HCl and subsequent evaporation is performed at temperatures higher than 173 K, the resulting IR absorption spectrum is significantly different to HCl · 6H$_2$O, as shown in Fig. 8. The peak at 3230 cm^{-1} decreases in intensity, but at the same time the whole O–H stretch region broadens upon uptake of HCl. The two small peaks above 3300 cm^{-1} are not visible anymore, as in the HH case, and collapse to a shoulder on the blue side of the 3230 cm^{-1} peak. The region between 1600–1800 cm^{-1} does not show distinct features, but rather displays a broad peak. This behavior is characteristic of a less ordered structure and is attributed to an amorphous or supercooled phase.

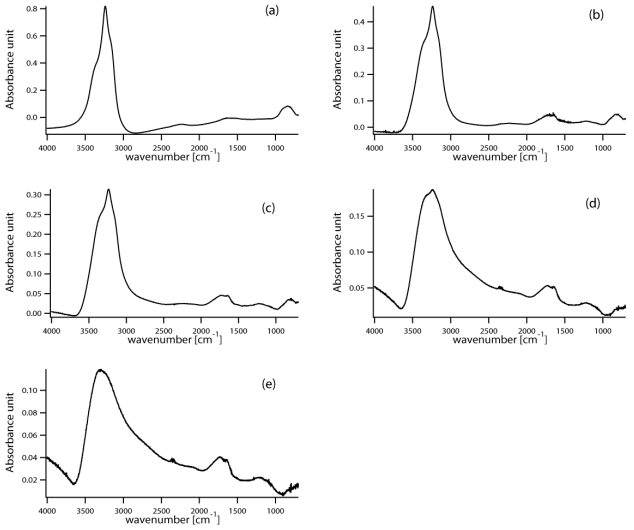

Fig. 8. IR spectra of an amorphous ice / HCl system obtained by doping pure ice **(a)** with HCl vapor at $T > 183$ K. **(b)**, **(c)**, **(d)** and **(e)** refer to successive scans after doping (260, 510, 650, 780 s, respectively) under SFR conditions.

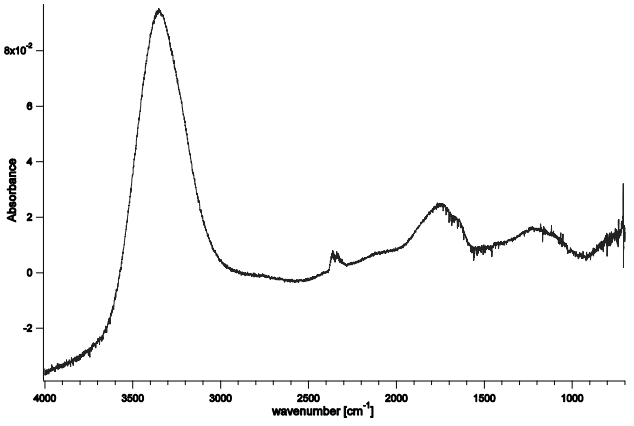

Fig. 9. IR absorption spectrum of an amorphous HCl–ice film obtained by deposition of a HCl–H_2O 1 : 10 mixture at 180 K.

During evaporation of water the HCl–H_2O film becomes more concentrated in HCl and the 3238 cm^{-1} peak becomes less prominent and finally indistinguishable from the broad peak in the 3000–3500 cm^{-1} region, but no frequency shift has been observed. In the final stages of evaporation (Fig. 8e), the spectrum resembles the one found in the literature for a 4 : 1 H_2O-to-HCl solid mixture (Xueref and Dominé, 2003; Ritzhaupt and Devlin, 1991) in the vicinity of 190 K. In some cases, a significant increase of the absorbance in the high energy wing (between 3500 and 4000 cm^{-1}) is an indication that the surface morphology of the film is rough, and therefore leads to light scattering. A similar phenomenon of surface roughening has been presented in a recent study (McNeill et al., 2006).

A further comparison may be made with respect to the spectrum of an amorphous HCl–ice system obtained by backfilling the chamber with a gaseous mixture of H_2O and HCl vapor in the ratio 10 : 1. A film grown in this fashion on the Si window at a temperature of 180 K shows features characteristic of a 4 : 1 mixture (see Fig. 9). The fact that the film is more concentrated in HCl in comparison to the injected initial gaseous mixture may be partially explained by the different values of the uptake probability γ of H_2O and HCl on ice, in analogy to the findings of Xueref and Dominé (2003). At 190 K γ_{HCl} on ice has a value of 0.34 (Flückiger et al., 1998), while γ_{H_2O} is approximately 0.25 for vapor-deposited ice (Pratte et al., 2005). However, the more important effect may well be the significantly smaller value of J_{ev}(HCl) compared to J_{ev}(H_2O) on such films as presented in Fig. 7. IR spectra obtained by codeposition of water and HCl vapor leading to amorphous mixtures are identical to those obtained by HCl doping of a pure ice film discussed above provided that the temperature is kept above 173 K. This points towards the thermodynamic stability of the amorphous thin film in this T range, which in addition is chemically more reactive than crystalline HCl · 6H_2O (McNeill et al., 2006).

3.5 Crystalline to amorphous transition

A number of experiments have addressed the stability of the crystalline HCl · 6H_2O structure. Pure HCl · 6H_2O films were grown as discussed above and the temperature was slowly raised under static conditions. In contrast to evaporation at $T = 187 \pm 0.5$ K (as displayed in Fig. 2), where the IR spectral shape does not change with decreasing film thickness, thermal decomposition occurs when the temperature is raised to 200 K under static conditions and the HCl partial pressure increases (Fig. 10). The spectrum of an initially pure HCl · 6H_2O film displayed in Fig. 10 shows a significant contamination by an amorphous phase, which is particularly evident in the 1600–1900 cm^{-1} region, where the sharp 1635 cm^{-1} peak becomes progressively less visible as the 1900 cm^{-1} absorption becomes broader and shifts towards lower wave numbers. The absorbance in the region around 1200 cm^{-1} decreases and tends to broaden. The overall O–H stretch region becomes broader, as in the amorphous case. We suggest that the IR absorption spectrum is due to the superposition of two separate contributions, namely crystalline HH and amorphous HCl–H_2O. Raising the temperature increases the amorphous component at the expense of crystalline HH.

The exact temperature at which the transition between the crystalline HH and the amorphous HCl–H_2O phase occurs depends on the particular experiment, especially on P(HCl), in agreement with the HCl–H_2O phase diagram: for SFR pumping conditions, the crystalline-to-amorphous phase transition begins to occur at 195 K. Owing to the HCl evaporation-induced irreversible decay of HH, the optical

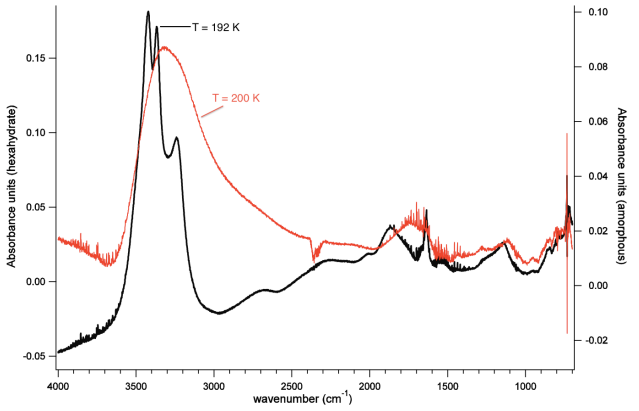

Fig. 10. IR spectrum of an initial HCl · 6H$_2$O film generated at 170 K using a dose leading to 8×10^{16} molecules of adsorbed HCl. The HH film was heated to 192 K (black trace) and subsequently to 200 K (red trace). This experiment was performed under static conditions.

density characteristic of HH already noticeably decreases at $T \geq 195$ K for static conditions as well, similar to SFR conditions. We reiterate that under static conditions, P_{eq}(HCl) may reach levels that are higher by 5 % compared to P_{ss}(HCl).

The IR spectrum of the amorphous mixture in Fig. 10 is somewhat distorted and in some regions (for $2500 < \nu/[\text{cm}^{-1}] < 3200$ and $\nu > 3600\,\text{cm}^{-1}$) looks like a first derivative of an absorption band. This phenomenon may be explained by anomalous dispersion of light on the film surface. The absorption spectrum may be corrected by employing the Kramers–Kronig relations to separate the n and k component of the complex index of refraction ($\tilde{n} = n + ik$), which takes into account refraction (n) and absorption (k), respectively. In our case, however, it would be difficult to apply this treatment for the reconstruction of the reflection spectrum from the observed transmission spectrum. Due to the sample preparation by backfilling, the present films grow on both faces of the Si window and therefore multiple reflections at each interface of the optical system vacuum–ice–Si–ice–vacuum should be taken into account. A similar treatment has been developed by Toon et al. (1994) that requires the knowledge of the refractive index of the thin film and the coherence degree: this last parameter, in particular, has not been determined in our experiment. We therefore present the raw recorded transmission spectra of Fig. 10 at 200 K and stress that anomalous dispersion of light on the film surface is only found in this case, and not at lower temperatures. This may mean that the HCl · 6H$_2$O film undergoes a phase transition that may lead to an increase in the surface roughness, probably leading to the formation of a highly granular structure that influences the optical properties of the film. This result is similar to the findings of McNeill et al. (2006). In that work, the roughening effect of HCl has been studied using an ellipsometric technique and a smooth transition between the crystalline and the liquid phases has been observed, visible by the progressive formation of a liquid-like layer on top of the film.

Figure 11 displays both the phase transition and the HH evaporation experiments as pathways in the HCl–H$_2$O phase diagram (Molina, 1994) that we have obtained under SFR conditions in addition to the ones at static conditions discussed above. The lines represent specific experimental pathways, with P_{ss}(HCl) generally increasing with increasing temperature. The squares refer to the presence of crystalline HCl · 6H$_2$O monitored by IR transmission, whereas the circles refer to the presence of amorphous HCl–H$_2$O. Because the phase transition takes some time at lower temperatures, we observe the coexistence of both HH and amHCl–H$_2$O during phase transition, which is marked by the juxtaposition of the blue squares (HH) and red circles (amHCl–H$_2$O). As previously pointed out, McNeill et al. (2006) found that only the innermost part of the "ice" region in the HCl–H$_2$O phase diagram is actually composed of a crystalline or "non-disordered" structure. The present observations confirm this by identifying the boundary region between pure "ice" and HCl · 6H$_2$O as an amorphous HCl–H$_2$O phase monitored by FTIR spectroscopy in transmission. Other researchers using different diagnostic methods have referred to this region of the HCl–H$_2$O phase diagram as a quasi-liquid layer or disordered structure (Molina, 1994; McNeill et al., 2006).

The green symbols in Fig. 11 pertain to HH evaporation experiments under SFR conditions in which the temperature was slowly raised. It seems that the low-temperature "starting point" of the experiment at the corresponding value of initial P_{ss}(HCl) determines the fate of the HH sample under SFR conditions and increasing temperature. The different initial conditions have been obtained by letting H$_2$O evaporate under SFR conditions for different lengths of time during HH preparation (see Sect. 2.2). On the one hand, the HH samples at high P_{ss}(HCl) correspond to a H$_2$O-deficient or pure HH sample (green points) and will evaporate akin to data shown in Fig. 2 without prior phase transition to amHCl–H$_2$O. On the other hand, the H$_2$O-rich HH samples at atmospherically relevant and thus low P_{ss}(HCl), represented by blue squares at low temperature, undergo a phase transition at increasing temperature to amHCl–H$_2$O (red circles in Fig. 11). According to Gibbs' phase rule we have a three-phase system (gas phase, crystalline ice and HH) of two chemically distinct components (HCl, H$_2$O) that will lead to a single degree of freedom, namely the composition of the condensed phase. We therefore conclude that the initial H$_2$O content of the mixed ice / HH system determines the fate at increasing temperature. Pure HH evaporates without phase transition, whereas water-rich HH undergoes a phase transition to amHCl–H$_2$O. The dividing line between the green and the blue/red symbols in Fig. 11 seems to be parallel to the ice–HH coexistence line and pegged to $P_{eq}(\text{HCl}) = 1.0 \times 10^{-7}$ Torr at 170 K. Whenever there is "excess" H$_2$O as in water-rich HH/ice, the evaporating HCl interacts with the ice and

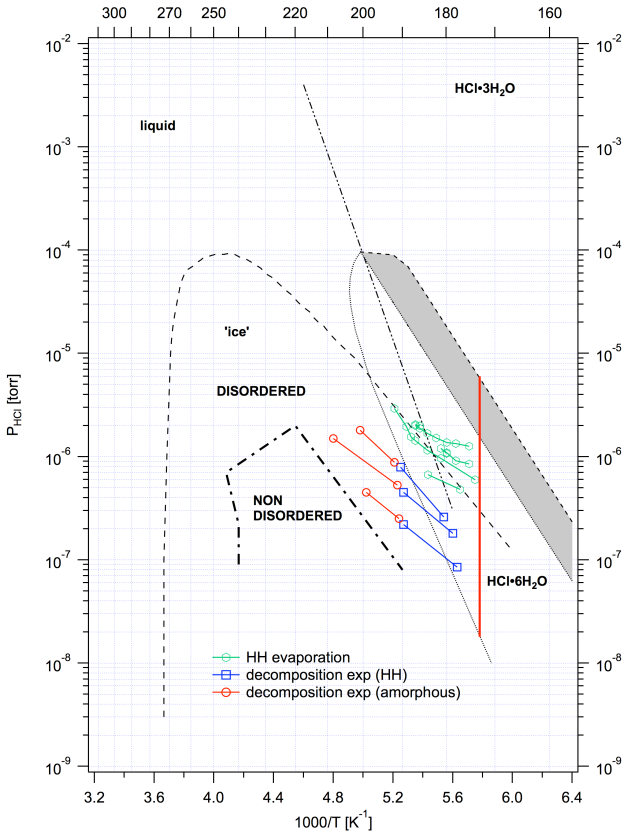

Fig. 11. Phase diagram for the binary system HCl–H_2O. The gray area for the HCl • 6H_2O existence is an extension of the existence area proposed by Iannarelli et al. (2013). The green circles represent HH evaporation, whereas the red circles (amorphous HCl–H_2O) and blue squares (crystalline HCl • 6H_2O) represent phase transition experiments. The colored lines represent individual experiments at stirred-flow conditions. The squares indicate the presence of a crystalline HCl • 6H_2O phase, while the circles represent amorphous HCl–ice as indicated by the corresponding FTIR spectra. The juxtaposition of red circles/blue squares in the "ice" existence area corresponds to simultaneous observations of HH and amHCl–H_2O. The vertical red bar at $T = 173$ K indicates the stability limit of HCl • 6H_2O. The disordered/non-disordered (crystalline) limit follows data by McNeill et al. (2006).

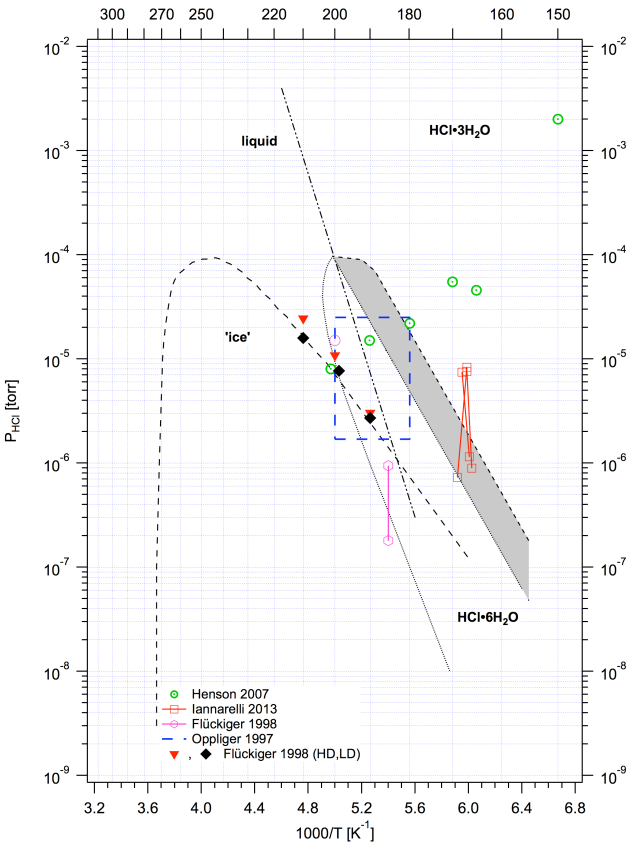

Fig. 12. Phase diagram for the binary system HCl–H_2O. The gray area for the HCl • 6H_2O existence is an extension of the existence area proposed by Iannarelli et al. (2013). The green points from Henson et al. (2007), the red squares from nucleation experiments performed by Iannarelli et al. (2013), the purple points from Flückiger et al. (1998) and the blue broken rectangle from Oppliger et al. (1997) are discussed in the text.

nucleates an amorphous HCl–H_2O phase that is more stable than HH.

As far as J_{ev}(HCl) is concerned, the kinetics of the phase transition HH amHCl–H_2O at increasing temperature may be described by the turnover from Eqs. (14)–(16) at approximately 195 K, as displayed in Fig. 7 and discussed in Sect. 3.3. Flückiger et al. (1998) measured both J_{ev}(HCl) and the corresponding HCl accommodation coefficient α_{HCl} or rate constant k_{ads} ($= k_{eff}$) for HCl adsorption on amHCl–H_2O using both continuous HCl dosing at steady state (k_{eff}) and real-time pulsed HCl admission in pulsed valve experiments (k_{ads}). Table 6 lists P_{eq}(HCl) in the range 190 to 210 K in both low-dose (LD) and high-dose (HD) experiments, typically corresponding to HCl doses of 5×10^{14} and 5×10^{15} molecule and higher, respectively. The steady-state experiments correspond to low-dose exposures. Flückiger et al. (1998) found that J_{ev}(HCl) was identical for both LD and HD experiments, whereas values for k_{ads} are different. HD experiments have a significantly smaller value for k_{ads} compared to LD experiments, hence their higher HCl vapor pressure, which puts them definitely into the true liquid region (inverted red triangles in Fig. 12). P_{eq}(HCl) as a function of T displayed in Table 6 identifies the pertinent region in the HCl–H_2O phase diagram displayed in Fig. 12 where the black diamonds and the inverted red triangles correspond to HCl LD and HD experiments. The phase diagram in Fig. 12 clearly shows that the HD experiments address the true liquid HCl–H_2O state, whereas those of LD pertain to the ice–liquid coexistence or "disordered state" region displayed in Fig. 11 and identified by McNeill et al. (2006). We therefore identify the green line in Fig. 7 with J_{ev}(HCl) for the "disordered state".

Table 6 also reveals the thermochemical parameters for HCl–H_2O explored by Flückiger et al. (1998) in the range 190–210 K. It is instructive to compare the heat of evaporation of HCl (ΔH_r^0 in Table 6) with the negative of the tabulated heats of solution of HCl at different solute concentrations (Wagman et al., 1982). From Table 6 we obtain $\Delta H_r^0 = -34.8$ and $-29.3\,\mathrm{kJ\,mol^{-1}}$ for HD and LD experiments, respectively, which corresponds to a H_2O / HCl ratio of 1.25 and 1 : 1 in solution at standard conditions. These concentrations correspond to a 61.5 and 66.7 % (wt) HCl–H_2O mixture for HD and LD experiments, respectively, in comparison to a saturated solution of 67.3 % (wt) at 4 °C (Perry's, 1997; Matheson, 1980). Owing to the high solubility of HCl in H_2O, the heat of solution strongly depends on HCl concentration and attains a value of $-74.87\,\mathrm{kJ\,mol^{-1}}$ at infinite dilution of HCl, roughly a factor of two higher than the heat of solution in the HD and LD experiments. Assuming that ΔH_r^0 does not substantially change with temperature relative to standard conditions, we conclude that for both types of experiments, a concentrated HCl–H_2O solution or phase is in equilibrium with the gas phase. Owing to the uncertainty of the relative thickness of the HCl–H_2O phase, we are unable to state at present whether or not the aqueous HCl concentration is significantly different between HD and LD experiments.

McNeill et al. (2006, 2007) connected reactivity and structural/morphological features of ice films for the first time. They have shown for the binary HCl–H_2O system that a large part of the "ice" existence area on the fringes to the solution coexistence line was disordered in nature, and thus perturbed by the presence of adsorbed HCl in a disordered state. As a result, heterogeneous reactions involving HCl occurred significantly faster in this region compared to the non-disordered – that is, crystalline – region in the core of the "ice" existence region. A case in point and a relevant example is Reaction (R1), which is the most important reaction in polar ozone depletion chemistry. In direct response to a query posed by McNeill et al. (2006), we ascertain that the rectangle represented by the blue dashed line in Fig. 12 was the area of the phase diagram explored by Oppliger et al. (1997) in which the large uptake coefficient γ_1 for Reaction (R1) had an inverse T dependence. Typically, γ_1 was in the range 0.14–0.24 and 0.26–0.34 at 200 and 180 K, respectively, for concurrent flow experiments of HCl and $ClONO_2$. The lower limit of the range corresponds to a stoichiometric flow of HCl, whereas the upper limit corresponds to an excess of HCl by a factor of three relative to $ClONO_2$. We conclude that the results obtained by Oppliger et al. (1997) are comparable to McNeill et al. (2006) for Reaction (R1) occurring in the disordered region of the HCl–H_2O phase diagram.

Regarding the uptake of HCl on ice (γ_{HCl}), Flückiger et al. (1998) obtained similarly large numbers for Reaction (R1), namely $\gamma_{HCl} = 0.50$ and 0.050 for the disordered state and the true liquid state at 185 K, respectively. In contrast, $\gamma_{HCl} = 0.025$ was measured for the true liquid state at 200 K. These kinetic values are presented here because fast laminar flow tube methods are not suitable to establish differences in large values of γ. Together with γ_1, the results on γ_{HCl} underline the strong tendency of pure ice to interact with HCl or to undergo a bimolecular heterogeneous reaction involving HCl in the disordered state. However, γ_{HCl} decreases roughly by an order of magnitude when HCl interacts with the true liquid state. The corresponding values of P_{eq}(HCl) of Flückiger et al. (1998) are displayed in Fig. 12 as purple symbols.

Finally, a comment on the often evoked nucleation barrier to HCl · 6H_2O shall be made that sometimes precludes the observation of HH despite the fact that the experimenter chooses the correct parameters for HH growth from the HCl–H_2O phase diagram (Foster et al., 1997). Henson et al. (2004, 2007) prepared high-surface-area amorphous ice deposited from vapor at 85 K and subsequently annealed samples using different protocols in order to obtain bulk ice samples whose BET surface area varied from 8 to $80\,\mathrm{m^2\,g^{-1}}$. After admitting controlled amounts of HCl, second harmonic generation (SHG) was used to monitor phase changes at the air–ice interface. Henson et al. (2004, 2007) identified the observed phase changes with the formation of HH at temperatures and P_{eq}(HCl) values where we either did not see formation of HH using FTIR absorption or where we observed too fast a decomposition of HH thin films according to Eq. (11). We were unable to nucleate HH at $T \geq 173$ K at P_{eq}(HCl) and P_{eq}(H_2O) used by Henson et al. (2004, 2007) where HH became unstable by undergoing a facile phase transition to the amorphous phase (see above). We are not questioning that phase transitions were in fact observed by these authors using SHG, but in the absence of positive (spectral) evidence for HH one must be careful with the interpretation of experiments that are not sufficiently specific for HH such as SHG. Figure 12 displays the nucleation conditions of Henson et al. (2004, 2007) as green points in addition to the observations of Iannarelli et al. (2013) using the identical experimental apparatus as in the present work. Especially the high values of P(HCl) would lead to a rapid phase transition to am(HCl–H_2O) in view of the results displayed in Fig. 11 (green points). Iannarelli et al. (2013) observed formation of HH on pure ice at $T \leq 173$ K at the conditions indicated by the red squares in Fig. 12. The upper three red squares represent P(HCl) at which nucleation of HH is first observed, and the lower red squares, each connected to the higher points at nucleation, correspond to P_{eq}(HH) values to which the system relaxes. It is clear that the temperature requirement for HH nucleation puts a severe constraint on HH observation in addition to the fact that P_{eq}(HCl) required for HH nucleation as indicated by the green points at 170 and 165 K is higher by roughly a factor of 5 to 10 compared to the experiments of Iannarelli (2013), who followed a similar experimental protocol as used in this work. It is therefore likely that Henson

Table 6. Thermodynamic data from van't Hoff plot for HCl evaporation of a HCl-doped H_2O–ice condensate whose evaporation flux J_{ev}(HCl) is displayed in Fig. 7 (data of Flückiger et al., 1998).

T/K	$(1/T)\cdot 10^3/K^{-1}$	$K_{ads} = k_{ads}/R^a_{des}$ P_{eq}/Torr (HD)[d]	lnK_{ads}(HD) /atm^{-1}[b]	$K_{ads} = k_{ads}/R^a_{des}$ P_{eq}/Torr (LD)[d]	lnK_{ads}(LD) /atm^{-1}[c]
210	4.762	$13.0/10.2\times10^{12}$ $2.44\ 10^{-5}$	17.25	$20.0/10.2\ 10^{12}$ 1.59×10^{-5}	17.69
200	5.000	$18.4/6.32\times10^{12}$ 1.08×10^{-5}	18.08	$25.8/6.32\ 10^{12}$ 7.69×10^{-6}	18.42
190	5.263	$28.0/2.73\times10^{12}$ 3.03×10^{-6}	19.34	$31.2/2.73\ 10^{12}$ 2.70×10^{-6}	19.45

[a] $(k_{ads}/R_{des})\cdot 2.44\times10^{19} = K_{ads}/\text{atm}^{-1}$ with k_{ads}/s^{-1} and R_{des}/molec cm^{-3} s^{-1} (Flückiger et al., 1998).
[b] $K_{ads}(\text{HD}) = (k_{ads}/R_{des})$ in units of atm, where k_{ads} is for high dose (HD) of typically 5×10^{15} molecule/pulse and higher. Corresponding thermochemical parameters are $\Delta H^0_r = -34.80$ kJ mol^{-1} and $\Delta S_r = -22.87$ J mol^{-1} K.
[c] $K_{ads}(\text{LD}) = (k_{ads}/R_{des})$ in units of atm, where k_{ads} is for low dose (LD) of typically 5×10^{14} molecule pulse^{-1}. Corresponding thermochemical parameters are $\Delta H^0_r = -29.30$ kJ mol^{-1} and $\Delta S_r = +7.20$ J mol^{-1} K.
[d] Calculated equilibrium vapor pressure according to $1/K_{ads}$ (Torr^{-1}) = P_{eq} / Torr.

et al. (2004, 2007) monitored the facile phase transition to amHCl–H_2O rather than formation of crystalline HH.

4 Atmospheric significance and conclusions

This study has addressed the behavior of thin vapor-deposited crystalline ice films of thicknesses in the micron range after exposure to HCl vapor at temperatures that are partly relevant to atmospheric processing. We have investigated the HCl–H_2O amorphous/supercooled and the crystalline HCl · 6H_2O structures. We have found that the nucleation of HCl · 6H_2O requires a high supersaturation ratio of HCl, on the order of 10 or higher for HCl vapor at $T \leq 173$ K, in agreement with previous studies (Ritzhaupt and Devlin, 1991; Koehler et al., 1993; Henson et al., 2004, 2007; Iannarelli et al., 2013). The structure of the ice film (amorphous, polycrystalline, I_h) to be doped by HCl is irrelevant for the formation and growth of HH. When HCl doping was performed at temperatures higher than 173 K, an amorphous HCl–H_2O phase was always obtained. For this reason we infer that nucleation of the HH phase will be difficult if not impossible under atmospheric conditions as UT/LS temperatures are rarely found to be less than 180 K. Pure amorphous samples obtained by doping ice films at temperatures higher than 173 K were never observed to crystallize to HH under the present experimental conditions. No changes in the IR spectrum of an amorphous HCl–H_2O sample were observed on the timescale of one hour at 187 K owing to the absence of HH nucleation. The high nucleation barrier requiring high supersaturation ratios of P_{eq}(HCl) is one of the reasons for the kinetic instability of HCl · 6H_2O under relevant atmospheric conditions. Evaporating HCl from crystalline HCl · 6H_2O is unable to regenerate crystalline HCl · 6H_2O when it condenses at the prevailing atmospheric temperatures. It appears therefore highly unlikely that amorphous HCl–H_2O will convert into crystalline HH under atmospheric conditions in the temperature range 180–200 K.

In most of the previous studies, crystallization of an HH thin film has been obtained at a temperature around 170 K by annealing amorphous ice samples that had been exposed to HCl vapors at temperatures lower than those used in the present study, extending to temperatures less than 100 K. In the present case, we found that HH can nucleate at $T \leq 173$ K on polycrystalline I_h ice. Therefore, the presence of amorphous ice rich in dangling OH bonds does not appear to be necessary in contrast to findings of McNeill et al. (2007). At temperatures below 173 K, nucleation occurred on the timescale of a few seconds and the HH key features were visible in the IR absorption spectrum at once. We avoided an excess of HCl over H_2O during nucleation of HH owing to the incidence of the facile phase transition to amorphous HCl–H_2O, and as such most runs were performed using an excess of H_2O over HCl. In order to obtain a stoichiometrically defined pure film of H_2O / HCl = 6 : 1, the evaporation of excess ice was therefore always required because the thin HH film considerably slowed down the diffusion of HCl to the underlying pure water ice.

The kinetic stability of the HCl · 6H_2O structure has been found to be limited to $T < 195$ K under SFR or static conditions, beyond which the decay of the crystalline structure to an amorphous one has been observed on the present timescale of a few minutes. The IR spectrum also presents scattering effects that occur beyond 3700 cm^{-1} due to the likely formation of a quasi-liquid or disordered phase on top of the ice film that has been observed during the transition of HH to the "ice" region in the HCl–H_2O phase diagram. This result confirms the findings of McNeill et al. (2006), which employed an elegant ellipsometric technique to demonstrate a roughening transition on ice upon HCl doping. The transition between the crystalline and the liquid phase has been attributed to the progressive formation of a liquid-like or amorphous layer on top of the ice film.

As a case in point we will consider the lifetime of a 10 µm diameter ice particle under UT/LS atmospheric conditions using the HCl evaporation flux J_{ev} of both an amorphous HCl–H_2O mixture and crystalline HH in comparison with

$J_{ev}(H_2O)$ of a pure water ice particle. We use a simple layer-by-layer model connected to a zero-order rate law for HCl and H_2O evaporation that expresses the time to complete evaporation θ, as displayed in Eq. (13):

$$\theta = ((\rho/M)N_A r)/J_{ev}(1 - \mathrm{rh}) \quad (13)$$

The parameters ρ, M, N_A, r and rh correspond to the specific density ($g\,cm^{-3}$), molecular weight (g), Avogadro's number, particle radius (cm) and relative humidity for the case of pure ice. The factor (1-rh) is valid for reversible adsorption/desorption kinetics of pure ice particles, whereas it is unity for amHCl–H_2O because of the absence of saturation of HCl uptake at UT/LS conditions. Once a formal ML of HCl has been adsorbed on ice, the uptake of HCl continues unabatedly, albeit at a reduced rate. For both HH and amHCl–H_2O HCl, uptake is not balanced by increasing evaporation of HCl because pure ice is increasingly dissolved in a phase transition in order to maintain an aqueous HCl solution of a given concentration. For pure ice, θ is infinity at 185 K and 18 min at 195 K for a 10 µm diameter particle at 15 km altitude (116.3 Torr total pressure). The frost point is at 1.7 ppm for 188 K and $P_{eq}(H_2O) = 5.2$ ppm at 195 K. Using the data displayed in Fig. 7, we obtain $\theta = 15.9$ h and 2.2 d for amHCl–H_2O and crystalline HH at 185 K, respectively, as well as $\theta = 7.9$ h for both HCl-containing solids at 195 K. It is obvious that the trends reflect the relative evaporation fluxes for HCl and H_2O with HCl evaporation being the rate-limiting step in all cases. Once HCl has evaporated, the remaining ice, devoid of HCl, will evaporate on a shorter timescale. The presence of HCl has a large stabilizing effect on the ice akin to HNO_3 regarding the total time to evaporation θ. In order to evaluate the fate of an atmospheric ice particle we need to consider both kinetic (J_{ev}) and thermodynamic aspects (phase diagram).

In summary, we have obtained the following results: (i) $HCl \cdot 6H_2O$ nucleation requires temperatures lower than 173 K to occur on vapor-deposited polycrystalline (hexagonal) ice films; (ii) at temperatures higher than 173 K only an amorphous HCl–H_2O mixture that does not crystallize to $HCl \cdot 6H_2O$ under any explored conditions is obtained upon dosing HCl on polycrystalline ice; (iii) the first pure $HCl \cdot 6H_2O$ FTIR spectra in transmission as well as mid-IR differential cross sections have been obtained; (iv) thermal decomposition of $HCl \cdot 6H_2O$ upon evaporation under SFR and static (equilibrium) conditions has been observed, which points towards kinetic instability of $HCl \cdot 6H_2O$ under the used experimental conditions; and (v) water-rich $HCl \cdot 6H_2O$ undergoes a facile phase transition towards an amorphous/supercooled phase at $T \geq 195$ K. In contrast, pure HH will preferentially lead to HCl evaporation and subsequent HH decay. The crystalline-to-amorphous phase transition in the range 190 to 195 K, with the probable formation of an amorphous HCl–H_2O layer on top of the film, occurs at a rate of approximately 0.5 to 2.5 molecular monolayers of HCl per second based on the rate of the rate-limiting step of HCl evaporation (Fig. 7). Appendix 3 (Supplement) gives the different values for formal HCl monolayer saturation on H_2O ice when results are coined in molecular monolayers of adsorbed HCl.

The four principal reasons for the anticipated absence of crystalline HH under atmospheric conditions are the following: (i) the high nucleation barrier owing to the required high value of $P_{eq}(HCl)$; (ii) the low nucleation temperature of $T \leq 173$ K; (iii) the facile phase transition of HH towards amHCl–H_2O under water-rich conditions; and (iv) irreversible decomposition of HH starting at 185 K through HCl evaporation, thus implying low kinetic stability of HH under UT/LS conditions and underlining the metastable nature of HH. These factors lead to a narrow window of crystalline HH stability in the range 173–185 K for HH if formed at all at UT/LS conditions. HH may therefore be regarded as a metastable phase for $T > 173$ K, as displayed by the vertical red line in Fig. 11.

Supplementary material related to this article is available online at http://www.atmos-chem-phys.net/13/11905/2013/acp-13-11905-2013-supplement.pdf.

Acknowledgements. Generous support for this research was provided by the Fonds National Suisse (Swiss National Science Foundation) under contract 200020-105471. We would like to thank R. Iannarelli for supporting experiments and calibrations as well as for help in setting up the templates of the redrawn binary HCl–H_2O phase diagram.

Edited by: V. F. McNeill

References

Abbatt, J. P. D., Beyer, K. D., Fucaloro, A. F., McMahon, J. R., Wooldridge, P. J., Zhang, R., and Molina, M. J.: Interaction of HCl vapor with water ice: implications for the stratosphere, J. Geophys. Res., 97, 15819–15826, 1992.

Banham, S. F., Sodeau, J. R., Horn, A. B., McCoustra, M. R. S., and Chesters, M. A.: Adsorption and ionization of HCl on an ice surface, J. Vac. Sci. Technol. A, 14, 1620–1626, 1996.

Bergren, M. S., Schuh, D., Sceats, M. G., and Rice, S. A.: The OH stretching region infrared spectra of low density amorphous solid water and polycrystalline ice Ih, J. Phys. Chem., 69, 3477–3482, 1978.

Borrmann, S., Solomon, S., Dye, J.E., and Luo, B. P.: The potential of Cirrus Clouds for heterogeneous Chlorine Activation, Geophys. Res. Lett., 23, 2133–2136, 1996.

Bournel, F., Mangeney, C., Tronc, M., Laffon, C., and Parent, P.: Acidity of hydrogen chloride at the surface of low-temperature (40–150 K) water-ice films, Phys. Rev. B, 65, 201404, 2002.

Buch, V. and Devlin, J. P.: Spectra of dangling OH bonds in amorphous ice assignment to 2- and 3-coordinated surface molecules, J. Chem. Phys., 94, 4091–4092, 1991.

Chaix, L., van den Bergh, H., and Rossi, M. J.: Real-Time Kinetic Measurements of the Condensation and Evaporation of D_2O on Ice at $140 < T/K < 220$, J. Phys. Chem. A, 102, 10300–10309, 1998.

Delval, C. and Rossi, M. J.: The kinetics of condensation and evaporation of H_2O from pure ice in the range 173–223 K: a quartz crystal microbalance study, Phys. Chem. Chem. Phys., 6, 4665–4676, 2004.

Delval, C. and Rossi, M. J.: Influence of monolayer amounts of HNO_3 on the evaporation rate of H_2O over ice in the range 179 to 208 K: A quartz crystal microbalance study, J. Phys. Chem. A, 109, 7151–7165, 2005.

Delval, C., Fluckiger, B., and Rossi, M. J.: The rate of water vapor evaporation from ice substrates in the presence of HCl and HBr: implications for the lifetime of atmospheric ice particles, Atmos. Chem. Phys., 3, 1131–1145, doi:10.5194/acp-3-1131-2003, 2003.

Delzeit, L., Rowland, B., and Devlin, J. P.: Infrared spectra of HCl complexed/ionized in amorphous hydrates and at ice surfaces in the 15–90 K range, J. Phys. Chem., 97, 10312–10318, 1993.

Flückiger, B., Thielmann, A., Gutzwiller, L., and Rossi, M. J.: Real time kinetics and thermochemistry of the uptake of HCl, HBr and HI on water ice in the temperature range 190 to 210 K, Ber. Bunsen. Phys. Chem., 102, 915–928, 1998.

Foster, K. L., Tolbert, M. A., and George, S. M.: Interaction of HCl with Ice: Investigation of the Predicted Trihydrate, Hexahydrate, and Monolayer Regimes, J. Phys. Chem. A, 101, 4979–4986, 1997.

Friedl, R. R., Goble, J. H., and Sander, S. P.: A Kinetics Study of the homogeneous and heterogeneous Components of the $HCl + ClONO_2$ Reaction, Geophys. Res. Lett. 13, 1351–1354, 1986.

Graham, J. D. and Roberts, J. T.: Interaction of HCl with crystalline and amorphous ice: implications for the mechanism of ice-catalyzed reactions, Geophys. Res. Lett., 22, 251–254, 1995.

Graham, J. D. and Roberts, J. T.: Formation of $HCl \cdot 6H_2O$ from ice and HCl under ultrahigh vacuum, Chemometr. Intell. Lab., 37, 139–148, 1997.

Hanson, D. R. and Mauersberger, K.: HCl / H_2O Solid Phase Vapor Pressures and HCl Solubility in Ice, J. Phys. Chem., 94, 4700–4705, 1990.

Hanson, D. R. and Ravishankara, A. R.: Investigation of the Reactive and Nonreactive Processes involving $ClONO_2$ and HCl on Water and Nitric Acid Doped Ice, J. Phys. Chem., 96, 2682–2691, 1992.

Haq, S., Harnett, J., and Hodgson, A.: Adsorption and solvation of HCl into ice surfaces, J. Phys. Chem. B, 106, 3950–3959, 2002.

Henson, B. F., Wilson, K. R., Robinson, J. M., Noble, C. A., Casson, J. L., and Worsnop, D. R.: Experimental isotherms of HCl and H_2O ice under stratospheric conditions: Connections between bulk and interfacial thermodynamics, J. Chem. Phys., 121, 8486–8499, 2004.

Henson, B. F., Wilson, K. R., Robinson, J. M., Nobel, C. A., Casson, J. L., Voss, L. F., and Worsnop, D. R.: Nucleation of Bulk Phases in the HCl/H_2O System, J. Phys. Chem. A, 111, 8635–8641, 2007.

Huthwelker, T., Malmström, M. E., Helleis, F., Moortgat, G. K., and Peter, T.: Kinetics of HCl Uptake on Ice at 190 and 203 K: Implications for the Microphysics of the Uptake Process, J. Phys. Chem. A, 108, 6302–6318, 2004.

Huthwelker, T., Ammann, M., and Peter, T.: The Uptake of Acidic Gases on Ice, Chem. Rev., 106, 1375–1444, 2006.

Hynes, R. G., Mössinger, J. C., and Cox, R. A.: The interaction of HCl with water-ice at tropospheric temperatures, Geophys. Res. Lett. 28, 2827–2830, 2001.

Hynes, R. G., Fernandez, M. A., and Cox, R. A.: Uptake of HNO_3 on water-ice and coadsorption of HNO_3 and HCl in the temperature range 210–235 K, J. Geophys. Res., 107, D244797, 2002.

Iannarelli, R. and Rossi, M. J.: H_2O and HCl trace gas kinetics on crystalline and amorphous HCl hydrates in the range 170 to 205 K: the HCl / H2O phase diagram revisited, Atmos. Chem. Phys. Discuss., 13, 30765–30839, doi:10.5194/acpd-13-30765-2013, 2013.

Jancso, G., Pupezin, J., and Van Hook, W. A.: The vapor pressure of ice between $+10^{-2}$ and -10^{+2}°, J. Phys. Chem., 74, 2984–2989, 1970.

Koehler, B. G., McNeill, L., Middlebrook, A. M., and Tolbert, M. A.: Fourier transform infrared studies of the interaction of HCl with model polar stratospheric cloud films, J. Geophys. Res., 98, 10563–10571, 1993.

Lee, S.-H., Leard, D. C., Zhang, R., Molina, L. T., and Molina, M. J.: The $HCl + ClONO_2$ reaction on various water ice surfaces, Chem. Phys. Lett. 315, 7–11, 1999.

Marti, J. and Mauersberger, K.: A survey and new measurements of ice vapor-pressure at temperatures between 170 and 250 K, Geophys. Res. Lett., 20, 363–366, 1993.

Matheson Gas Data Book, 6th edition, second printing, Braker, W. and Mossman, A. L. (Eds.), Matheson Gas Products, Secaucus, NJ 07094, 1980.

Martín-Llorente, B., Fernández-Torre, D., Herrero, V. J., Ortega, I. K., Escribano, R., and Maté, B.: Vibrational spectra of crystalline hydrates of atmospheric relevance: Bands of hydrated protons, Chem. Phys. Lett., 427, 300–304, 2006.

McNeill, V. F., Loerting, T., Geiger, F. M., Trout, B. L., and Molina, M. J.: Hydrogen chloride-induced surface disordering on ice, P. Natl. Acad. Sci., 103, 9422–9427, 2006.

McNeill, V. F., Geiger, F. M., Loerting, T., Trout, B. L., Molina, L. T., and Molina, M. J., Interaction of Hydrogen Chloride with Ice Surfaces: The Effects of Grain Size, Surface Roughness, and Surface Disorder, J. Phys. Chem. A, 111, 6274–6284, 2007.

Molina, L. T., Molina, M. J., Stachnik, R. A., and Tom, R. D.: An Upper Limit to the Rate of the $HCl + ClONO_2$ Reaction J. Phys. Chem., 89, 3779–3781, 1985.

Molina, M. J.: The probable role of stratospheric "ice" clouds: heterogeneous chemistry and the "ozone hole", in The Chemistry of the atmosphere: its impact on global change, IUPAC Chemrawn VII Conference, Blackwell Scientific Publications, Boston, chapter 3, 27–38, 1994.

Molina, M. J., Tso, T. L., Molina, L. T., and Wang, F. C. Y.: Antarctic Stratospheric Chemistry of Chlorine Nitrate, Hydrogen Chloride and Ice: Release of Active Chlorine, Science, 238, 1253–1257, 1987.

Oppliger, R., Allanic A., and Rossi, M. J.: Real-Time Kinetics of the Uptake of $ClONO_2$ on Ice and in the Presence of HCl in the Temperature Range $160 \leq T/K \leq 200$, J. Phys. Chem. A, 101, 1903–1911, 1997.

Ortega, I. K., Escribano, R., Fernández-Torre, D., Herrero, V. J., Maté, B., and Moreno, M. A.: The HCl hexahydrate : RAIR

spectra and theoretical investigation, Chem. Phys. Lett., 396, 335–340, 2004.

Ortega, I. K., Escribano, R., Herrero, V. J., Maté, B., and Moreno, M. A.: The structure and vibrational frequencies of crystalline HCl trihydrate, J. Mol. Struct., 742, 147–152, 2005.

Ortega, I. K., Escribano, R., Fernández-Torre, D., Herrero, V. J., Maté, B., and Moreno, M. A.: Exposure of nitric acid trihydrate crystals to HCl: a spectroscopic study, J. Geophys. Res., 111, D13206, doi:10.1029/2005JD006931, 2006.

Parent, P. and Laffon, C.: Adsorption of HCl on the water ice surface studied by x-ray absorption spectrsocopy, J. Phys. Chem. B, 109, 1547–1553, 2005.

Perry's Chemical Engineers' Handbook, 7th edition, Perry, R. H., Green, D. W., and Maloney, J. O. (Eds.), McGraw-Hill, chapter 2, p. 127, 1997.

Pratte, P., van den Bergh, H., and Rossi, M. J.: The kinetics of H_2O vapor condensation and evaporation on different types of ice in the range 130–210 K, J. Phys. Chem. A, 110, 3042–3058, 2006.

Ritzhaupt, G. and Devlin, J. P.: Infrared spectra of nitric and hydrochloric acid hydrate thin films, J. Phys. Chem., 95, 90–95, 1991.

Sadtchenko, V., Giese, C. F., and Gentry, W. R.: Interaction of hydrogen chloride with thin ice films: the effect of ice morphology and evidence for unique surface species on crystalline vapor-deposited ice, J. Phys. Chem. B, 104, 9421–9429, 2000.

Solomon, S.: Progress towards a quantitative understanding of Antarctic ozone depletion, Nature, 347, 347–354, 1990.

Solomon, S., Borrmann, S., Garcia, R. R., Portmann, R., Thomason, L., Poole, L. R., Winker, D., and McCormick, M. P.: Heterogeneous Chlorine Chemistry in the Tropopause Region, J. Geophys. Res.-Atmos., 102, 21411–21429, 1997.

Thibert, E. and Dominé, F.: Thermodynamics and kinetics of the solid solution of HCl in ice, J. Phys. Chem. B, 101, 3554–3565, 1997.

Toon, O. B., Tolbert, M. A., Koehler, B. G., Middlebrook, A. M., and Jordan, J.: Infrared optical constants of H_2O ice, amorphous nitric acid solutions, and nitric acid hydrates, J. Geophys. Res., 99, 631–654, 1994.

Uras-Aytemiz, N., Joyce, C., and Devlin, J. P.: Kinetics of ice particle conversion to the hydrates of HCl, J. Phys. Chem. A, 105, 10497–10500, 2001.

Vuillard, G.: Contribution A L'Etude de l'Etat Vitreux Et De La Cristallisation Des Solutions Aqueuses, Ann. Chim. 13, 233–297, 1957.

Wagman, D. D., Evans, W. H., Parker, V. B., Schumm, R. H., Halow, I., Bailey, S., Churney, K. L., and Nuttall, R. L.: The NBS tables of chemical thermodynamic properties, Selected values for inorganic and C_1 and C_2 organic substances in SI units, J. Phys. Chem. Ref. Data, 11, Suppl. No. 2, 1982.

Wooldridge, P. J., Zhang, R., and Molina, M. J.: Phase Equilibria of H_2SO_4, HNO_3, and HCl hydrates and the composition of polar stratospheric clouds, J. Geophys. Res. 100, 1389–1396, 1995.

Xueref, I. and Dominé, F.: FTIR spectroscopic studies of the simultaneous condensation of HCl and H_2O at 190 K – Atmospheric applications, Atmos. Chem. Phys., 3, 1779–1789, doi:10.5194/acp-3-1779-2003, 2003.

Zondlo, M. A., Hudson, P. K., Prenni, A. J., and Tolbert, M. A.: Chemistry and microphysics of polar stratospheric clouds and cirrus clouds, Annu. Rev. Phys. Chem., 51, 473–499, 2000.